Nation Cheng Kung University
Institute of Space and Plasma Sciences
113 Annual Report

研究生 ： 畢永葳 Yung-Wei Pi

指導教授 ： 張博宇 Po-Yu Chang

Data: 2024/01/22

Abstract

This report summarizes the activities carried out from 2024 to January 22, 2025. The main focus was on designing the current profile of the central solenoid of Formosa Integrated Research Spherical Tokamak (FIRST) that can provide enough loop voltage for breakdown and drive the plasma current too 100 kA and thus heat the plasma to 100 eV. The models include calculating the resistance and self-inductance of FIRST components and the mutual inductance between them, the eddy currents induced in the inner and outer vacuum vessel walls by the central solenoid, the loop voltage induced by the central solenoid with the effects of eddy currents in these walls, and plasma parameters, such as plasma current and temperature, as they vary over time due to ohmic heating from the central solenoid. It was found that the influence of the eddy current on the loop voltage induced by the central solenoid decreases to approximately 5% within 5 ms. Therefore, the duration of the central solenoid's current should be designed to exceed this time frame to minimize the effects of the eddy current. Additionally, to induce a 10 V loop voltage at a pressure of 10^{-5} Torr and a connection length of 1534 m, the central solenoid's maximum current must exceed 20 kA. Alternatively, if the central solenoid's current decreases linearly from 10 kA to 0 within 10 ms, the plasma current can exceed 100 kA for both 10^{-4} Torr and 10^{-5} Torr of background pressure, achieving the target current. While the plasma temperature exceeds the target of 100 eV for 10^{-5} Torr, it only reaches 40 eV for 10^{-4} Torr. Therefore, these models will be utilized to optimize the central solenoid's current profile to achieve the desired plasma temperature (100 eV) and current (100 kA). In conclusion, this report includes methods for calculating eddy currents, loop voltage, and plasma parameters in the Tokamak device

Contents

1. Formosa Integrated Research Spherical Tokamak (FIRST)

A Tokamak is a device used to achieve nuclear fusion through magnetic-confinement fusion (MCF). Our tokamak, Formosa Integrated Research Spherical Tokamak (FIRST), is the first Tokamak designed in Taiwan, and it will be built by 2026. The major and minor radii of plasma in FIRST are 45 cm and 32 cm, respectively. The elongation will be 2.4 so that the long and short radius of the plasma cross section is 76.8 cm and 32 cm, respectively. The vacuum vessel is approximately elliptical in shape, featuring an arc radius of 96.8 cm as shown in Figure 1-1. The center of the arc is 14 cm away from the z axis of the system. The device will provided a toroidal magnetic field of 0.5 T and a plasma current of 100 kA will be generated.

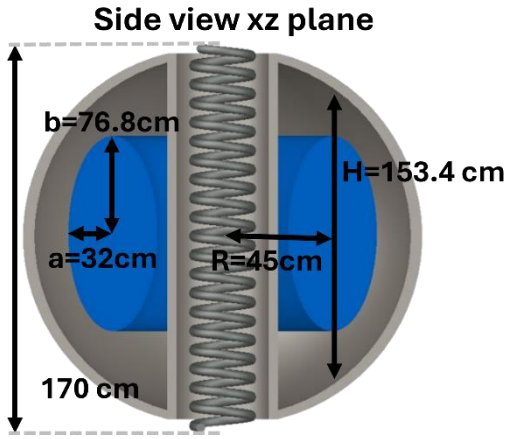

Figure 1-1: Simplified xz-plane cross-section of FIRST

FIRST employs a central solenoid (CS) with two layers, each comprises 140 turns, to produce a time-varying magnetic field. This field induces a loop voltage that generates plasma, drives the plasma current, and heats the plasma through ohmic heating. Using Townsend theory, we can calculate the required loop voltage for plasma generation under different background pressures, connection lengths, and positions within the Tokamak. Once the loop voltage is determined, we can assume breakdown has occurred, and plasma has been generated. By applying various theoretical models, such as the Collisional-Radiative Model and the electron energy balance equation, we can calculate how plasma parameters evolve over time due to ohmic heating from the

central solenoid. These calculations are essential for determining the device's specifications and ensuring its optimal design.

When the loop voltage is generated due to the time-varying magnetic field, the central solenoid also induces eddy currents in other components, such as the inner and outer vacuum vessel walls. These eddy currents lead to deviations in the calculated magnetic fields, impacting the accuracy of the design. Therefore, it is crucial to calculate the induced currents within the components and incorporate them into the design calculations to obtain more precise results.

This report consists of five sections: (1) calculation of the eddy current in the inner and outer vacuum vessel walls; (2) loop voltage calculation; (3) calculation of the evolution of plasma parameters; (4) future work; and (5) conclusion.

2. Calculation of the eddy currents in the inner and outer vacuum vessel walls

In the Tokamak device, we generate plasma, drive plasma current, and control plasma shape by adjusting the time-varying currents in coils such as poloidal field coil (PFC), toroidal field coil (TFC), and central solenoid (CS). However, the time-varying magnetic fields generated by these coils will induce eddy currents in vacuum vessel walls, which can negatively impact the originally calculated magnetic fields. Therefore, before constructing the Tokamak device, it is necessary to include the eddy currents within the device in the design to obtain more accurate results.

This section consists of six subsections: (1) the full circuit equation; (2) precondition conjugate gradient (PCG) method; (3) components defined in the calculation; (4) calculation of inductance and resistance of each element; (5) calculated results; and (6) conclusion.

2.1. The full circuit equation

To calculate the eddy current in the vacuum vessel wall, we can treat the vacuum vessel wall as a "coil". Then, the eddy current in the vacuum vessel wall can be calculated using the mutual inductance between the vacuum vessel wall and the central solenoid. To calculate the spatial profile of the eddy current, we use many ring coils stacking on top of each other to represent the vacuum vessel wall. Then, by calculating the induced current in each ring coil, we can calculate the eddy current at different locations using the full circuit equation [2]:

$$V = M\frac{dI}{dt} + RI. \tag{1}$$

Here, V represents voltage, I represents current, M represents inductance, and R represents resistance. This equation states that the total voltage "V" in a closed loop equals its induced voltage *"*$M\frac{dI}{dt}$*"* plus the voltage drop due to resistance *"*RI*"*. In the

next section, plasma is treated as a ring coil and can be included in the calculation.

For convenience in calculations, we have *V* and *I* in the vector form to represent voltages and currents in each coil and each vacuum vessel component. On the other hand, *M* and *R* are written in the matrix form including the self-inductance and the resistance of each coil and each vacuum vessel component, and the mutual inductance between each component. In addition, we use subscribes c, v, p to represent different type of components. Subscribe c represents coils in the Tokamak device, such as the central solenoid, PFC, and TFC; subscribe v represents components in the Tokamak device's vacuum vessel; subscribe p represents the plasma. Therefore, $\vec{I}$ is a column vector of size $n+1$, representing the currents of the total n components of coils and vacuum vessel components in the Tokamak device plus the plasma current; $\vec{V}$ is also a column vector of size $n+1$, representing the external voltages applied to the total n components of coils and vacuum vessel components in the Tokamak device plus the loop voltage of plasma; $\overleftrightarrow{R}$ is a diagonal matrix of size$(n+1)\times(n+1)$, representing the electrical resistance of the total n components of coils and vacuum vessel components plus the plasma; $\overleftrightarrow{M}$ is a symmetric matrix of size $(n+1)\times(n+1)$, representing the self-inductance (diagonal elements) and mutual inductance (off-diagonal elements) of the total n components of coils and vacuum vessel components plus plasma. Therefore, Eq.(1) can be written explicitly as:

$$\vec{V} = \overleftrightarrow{M}\frac{d\vec{I}}{dt} + \overleftrightarrow{R}\vec{I}$$

$$\Rightarrow \begin{bmatrix} V_{c1} \\ V_{c2} \\ \vdots \\ V_{v1} \\ V_{v2} \\ \vdots \\ V_{p} \end{bmatrix} = \begin{bmatrix} L_{c1} & M_{c1,c2} & M_{c1,c3} & \cdots & M_{c1,v1} & M_{c1,v2} & M_{c1,v3} & \cdots & M_{c1,p} \\ M_{c2,c1} & L_{c2} & M_{c2,c3} & \cdots & M_{c2,v1} & M_{c2,v2} & M_{c2,v3} & \cdots & M_{c2,p} \\ M_{c3,c1} & M_{c3,c2} & L_{c3} & \cdots & M_{c3,v1} & M_{c3,v2} & M_{c3,v3} & \cdots & M_{c3,p} \\ \vdots & \vdots & \vdots & \vdots & \vdots & \vdots & \vdots & \vdots & \vdots \\ M_{v1,c1} & M_{v1,c2} & M_{v1,c3} & \cdots & L_{v1} & M_{v1,v2} & M_{v1,v3} & \cdots & M_{v1,p} \\ M_{v2,c1} & M_{v2,c2} & M_{v2,c3} & \cdots & M_{v2,v1} & L_{v2} & M_{v2,v3} & \cdots & M_{v2,p} \\ M_{v3,c1} & M_{v3,c2} & M_{v3,c3} & \cdots & M_{v3,v1} & M_{v3,v2} & L_{v3} & \cdots & M_{v3,p} \\ \vdots & \vdots & \vdots & \vdots & \vdots & \vdots & \vdots & \vdots & \vdots \\ M_{p,c1} & M_{p,c2} & M_{p,c3} & \cdots & M_{p,v1} & M_{p,v2} & M_{p,v3} & \cdots & L_{p} \end{bmatrix} \begin{bmatrix} I'_{c1} \\ I'_{c2} \\ \vdots \\ I'_{v1} \\ I'_{v2} \\ \vdots \\ I'_{p} \end{bmatrix}$$

$$+ \begin{bmatrix} R_{c1} & 0 & \cdots & 0 & 0 & \cdots & 0 \\ 0 & R_{c2} & \cdots & 0 & 0 & \cdots & 0 \\ \vdots & \vdots & \vdots & \vdots & \vdots & \vdots & \vdots \\ 0 & 0 & \cdots & R_{v1} & 0 & \cdots & 0 \\ 0 & 0 & \cdots & 0 & R_{v2} & \cdots & 0 \\ \vdots & \vdots & \vdots & \vdots & \vdots & \vdots & \vdots \\ 0 & 0 & \cdots & 0 & 0 & \cdots & R_{p} \end{bmatrix} \begin{bmatrix} I_{c1} \\ I_{c2} \\ \vdots \\ I_{v1} \\ I_{v2} \\ \vdots \\ I_{p} \end{bmatrix}. \quad (2)$$

Eq.(1) can be solved numerically using finite difference method:

$$\vec{V} = \overleftrightarrow{M}\frac{d\vec{I}}{dt} + \overleftrightarrow{R}\vec{I} \Rightarrow \vec{V} = \overleftrightarrow{M}\frac{\vec{I'} - \vec{I}}{\Delta t} + \overleftrightarrow{R}\vec{I}$$

$$\Rightarrow \vec{V} = \overleftrightarrow{M}\frac{\vec{I'}}{\Delta t} - \overleftrightarrow{M}\frac{\vec{I}}{\Delta t} + \overleftrightarrow{R}\vec{I} = \overleftrightarrow{M}\frac{\vec{I'}}{\Delta t} + \left(\overleftrightarrow{R} - \frac{\overleftrightarrow{M}}{\Delta t}\right)\vec{I} \Rightarrow \frac{\overleftrightarrow{M}}{\Delta t}\vec{I'} = \vec{V} + \left(\frac{\overleftrightarrow{M}}{\Delta t} - \overleftrightarrow{R}\right)\vec{I}$$

$$\Rightarrow \vec{I'} = \left(\frac{\overleftrightarrow{M}}{\Delta t}\right)^{-1}\left[\vec{V} + \left(\frac{\overleftrightarrow{M}}{\Delta t} - \overleftrightarrow{R}\right)\vec{I}\right]. \quad (3)$$

In Eq. (3), $\vec{I'}$ represents the current in the following time step of $\vec{I}$,Notice that matrix $\overleftrightarrow{M}$ and $\overleftrightarrow{R}$ are constants when plasma is not included, since each coil and each vacuum vessel component will be fixed once the Tokamak is built. By proving $\vec{V}(t)$, we can obtain $\vec{I}(t)$ at any time.

When using the full circuit equation to calculate the eddy currents induced by the central solenoid in the vacuum vessel walls, the feedback effect of the eddy currents on the induced current in the central solenoid is negligible. This is because the eddy currents are relatively small compared to the central solenoid's driving current. To simplify the calculations and enhance computational efficiency, we disregard this feedback effect in our calculation as shown in Eq.(4).

Our current calculations only include the central solenoid (subscript cs), the vacuum vessel walls (subscript v), and the plasma (subscript p). Therefore, Eq. (4) only accounts for these components.

As mentioned earlier, V represents the external voltage. Since the vacuum vessel walls and plasma are passive elements, which don't have an independent external voltage source, their voltage is set to V = 0. However, to isolate the central solenoid from the direct calculation, we treat its induced effect on the other components as their respective source term. This induced effect is expressed as the mutual inductance between each component and central solenoid times the rate of change of the central solenoid's current. For example, as shown in Eq. (4), $M_{\mathrm{v1,cs}} \cdot \frac{dI_{cs}}{dt}$ represents the induced voltage from the central solenoid on the first vacuum vessel wall component.

$$\begin{bmatrix} V_{\mathrm{v1}} \\ V_{\mathrm{v2}} \\ \vdots \\ V_{\mathrm{p}} \end{bmatrix} = \begin{bmatrix} M_{\mathrm{v1,cs}} \\ M_{\mathrm{v2,cs}} \\ M_{\mathrm{v3,cs}} \\ \vdots \\ M_{\mathrm{p,cs}} \end{bmatrix} \frac{dI_{cs}}{dt} = \begin{bmatrix} L_{\mathrm{v1}} & M_{\mathrm{v1,v2}} & M_{\mathrm{v1,v3}} & \cdots & M_{\mathrm{v1,p}} \\ M_{\mathrm{v2,v1}} & L_{\mathrm{v2}} & M_{\mathrm{v2,v3}} & \cdots & M_{\mathrm{v2,p}} \\ M_{\mathrm{v3,v1}} & M_{\mathrm{v3,v2}} & L_{\mathrm{v3}} & \cdots & M_{\mathrm{v3,p}} \\ \vdots & \vdots & \vdots & \vdots & \vdots \\ M_{\mathrm{p,v1}} & M_{\mathrm{p,v2}} & M_{\mathrm{p,v3}} & \cdots & L_{\mathrm{p}} \end{bmatrix} \begin{bmatrix} I'_{\mathrm{v1}} \\ I'_{\mathrm{v2}} \\ \vdots \\ I'_{\mathrm{p}} \end{bmatrix} + \begin{bmatrix} R_{\mathrm{v1}} & 0 & \cdots & 0 \\ 0 & R_{\mathrm{v2}} & \cdots & 0 \\ \vdots & \vdots & \vdots & \vdots \\ 0 & 0 & \cdots & R_{\mathrm{p}} \end{bmatrix} \begin{bmatrix} I_{\mathrm{v1}} \\ I_{\mathrm{v2}} \\ \vdots \\ I_{\mathrm{p}} \end{bmatrix}. \quad (4)$$

To solve Eq.(4) numerically, precondition conjugate gradient (PCG) method is used, which will be introduced in next subsection.

2.2. Precondition conjugate gradient (PCG) method

Currently, in our calculation the matrix consists of 1125 components, and its size will continue to grow as more components are included in the calculation. This increase in matrix size will lead to greater computational complexity and longer computation times. To efficiently handle these challenges, instead of using conventional iterative methods, we employ the Preconditioned Conjugate Gradient (PCG) method [3].

The Preconditioned Conjugate Gradient (PCG) method is an optimization of the standard Conjugate Gradient (CG) method, which is widely used to solve large sparse symmetric positive-definite (SPD) linear systems. In our eddy current calculations, the inductance matrix $\vec{\vec{M}}$ is large, sparse, and poorly conditioned, making direct solvers like Gaussian elimination or LU decomposition inefficient due to high memory and computational costs.

While traditional iterative methods, such as Jacobi, Gauss-Seidel, or standard CG, can be used, their convergence speed heavily depends on the condition number of the matrix. Poorly conditioned matrices result in slow convergence, requiring many iterations to reach an accurate solution.

To improve efficiency, PCG introduces a preconditioner matrix H, which helps transform the original system:

$$Ax = B, \tag{5}$$

into a better-conditioned system:

$$H^{-1}Ax = H^{-1}B, \tag{6}$$

where A is corresponding to $\left(\frac{\vec{\vec{M}}}{\Delta t}\right)$ in Eq. (3), x is corresponding to $\vec{I'}$, and B is corresponding to $\left[\vec{V} + \left(\frac{\vec{\vec{M}}}{\Delta t} - \vec{\vec{R}}\right)\vec{I}\right]$.

A better-conditioned system refers to a transformed system where the condition number of the matrix is lower, meaning that the system is more numerically stable and that iterative solvers can converge faster. The condition number of a matrix A, denoted as $\kappa(A)$, measures how sensitive the solution x is to small changes in B. A high condition number leads to slow convergence and potential numerical errors, while a lower condition number means fewer iterations are needed for an accurate solution.

In practical computations, the condition number can be estimated using the singular value decomposition (SVD):

$$\kappa(A) = \frac{\sigma_{max}(A)}{\sigma_{min}(A)}, \tag{7}$$

where $\sigma_{max}(A)$ and $\sigma_{max}(A)$ are the largest and smallest singular values of A, respectively. A large $\kappa(A)$ indicates an ill-conditioned system, where numerical instability can arise, leading to slow convergence in iterative solvers like CG or PCG. To improve conditioning, preconditioning is used to transform the system into one with a lower condition number, enabling faster convergence.

Here, H is not exactly A^{-1} but rather an approximate inverse that improves the conditioning of the system. Directly computing A^{-1} would be computationally expensive and numerically unstable for large systems. Instead, H is chosen to approximate A^{-1} in a way that significantly reduces the condition number of A while being computationally efficient and easier to store.

By improving the condition number, PCG accelerates convergence, reducing the number of iterations needed while maintaining numerical stability. This is crucial as our matrix size increases with more calculated components, ensuring the calculation remains scalable and efficient.

2.3. Components defined in the calculation

FIRST primarily relies on the time-varying current in the central solenoid (indicated by the blue arrow in Figure 2-1) for plasma generation and driving plasma currents (represented by the orange arrow in Figure 2-1). Consequently, the central solenoid undergoes significant current variations that induce currents in the surrounding components, e.g. the vacuum vessel walls. As the vacuum vessel walls are the primary components affected and the main carrier of eddy currents, we first focus on calculating the eddy currents in the inner and outer vacuum vessel walls (depicted by the green and yellow arrows, respectively, in Figure 2-1) generated by the time-varying current of the central solenoid.

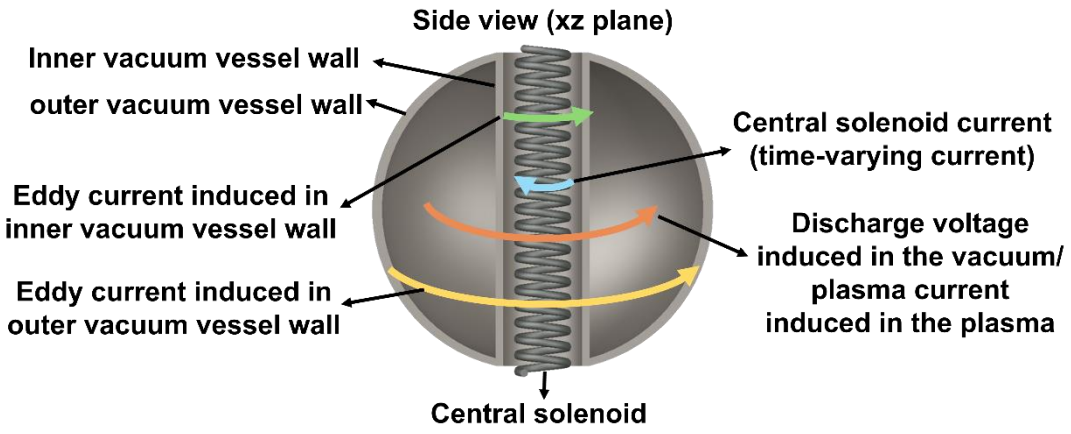

Figure 2-1: Schematic diagram of currents

As shown in Figure 2-2 (a), the central solenoid consists of two layers, each containing 140 turns, for a total of 280 turns. The distances from the centerline to the centers of the inner and outer layers are 88 mm and 100 mm, respectively. For simplicity, the major radius of the central solenoid in our calculations is set as their average, 94 mm.

The solenoid coil is a hollow copper tube wrapped with an insulating layer on the outside. The blue circle represents the insulation layer, which is 1 mm thick. The black circle represents the coil, with a diameter of 10 mm. The gray circle represents the hollow section for cooling water, with a diameter of 7.6 mm.

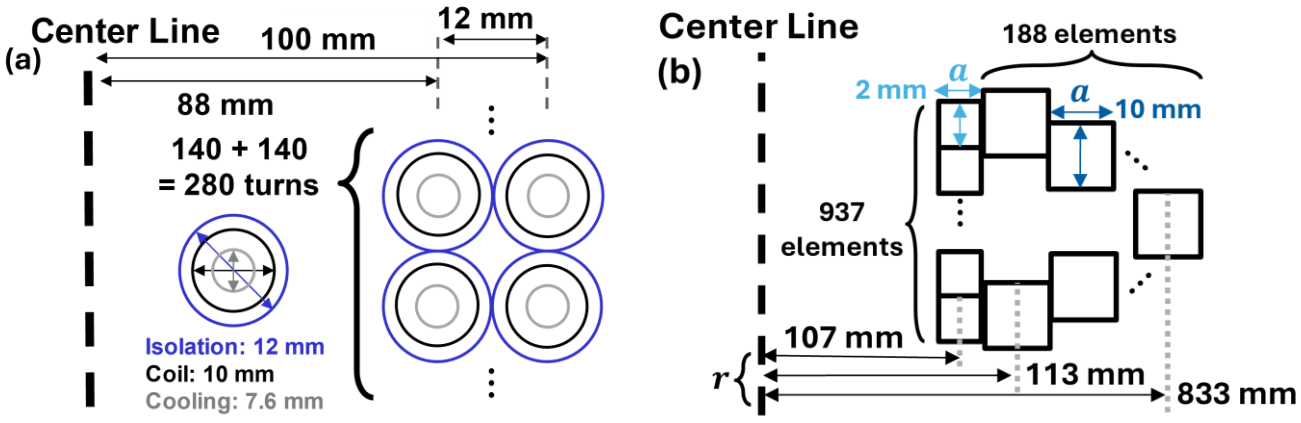

Figure 2-2: (a) Specifications of the central solenoid; (b) Specifications of the inner and outer vacuum vessel walls divided for calculation

For the vacuum vessel, we divide it into two parts: the inner vacuum vessel wall and the outer vacuum vessel wall, as shown in Figure 2-3. The curve of the outer

vacuum vessel wall, which is approximately elliptical in shape, centered at x = -140 mm, with an arc radius of 968 mm, is calculated based on the equation:

$$(r + 140)^2 + z^2 = 968^2. \quad (8)$$

The vacuum vessel wall is treated as many ring coils stacking on top of each other. To enhance calculation accuracy, as illustrated in Figure 2-2 (b), we divide the inner vacuum vessel wall into 937 identical ring coils with square cross-sections of 2 mm in each side, stacked together. Similarly, the outer vacuum vessel wall is divided into 188 ring coils with square cross-sections of 10 mm in each side and with different ring radius, stacked together. This segmentation allows for precise modeling of the eddy currents generated within the vacuum vessel walls.

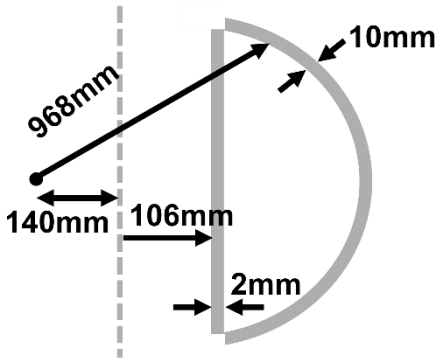

Figure 2-3: Specifications of the vacuum vessel

2.4. Calculation of inductance and resistance of each element

Before calculating the induced currents, we first need to compute the resistance and self-inductance of the central solenoid and vacuum vessel walls, as well as the mutual inductance between them.

This subsection consists of three subsubsections: (1) calculation of the resistance; (2) calculation of self-inductance; and (3) calculation of mutual inductance.

2.4.1. Calculation of the resistance

We use the resistance formula to calculate the resistance of the components:

$$R = \eta \frac{L}{A} \quad (9)$$

where R is the coil resistance, η is the resistivity of the material, L is the length of the coil, A is the cross-sectional area of the coil.

For the central solenoid, we first divide it into inner and outer layers and treat each turn within each layer as a single ring coil:

$$R_{\text{cs\_each}} = \eta_{\text{copper}} \frac{L_{\text{cs\_each}}}{A_{\text{cs\_each}}} = \eta_{\text{copper}} \frac{2\pi r_{\text{cs\_each}}}{\pi a_{\text{cs\_each}}^2 - \pi a_{\text{cooling}}^2} \tag{10}$$

where $R_{\text{cs\_each}}$ is the resistance of a single coil in the inner or outer layer, η_{copper} is the resistivity of copper $(1.68 \times 10^{-8}\ \Omega \cdot \text{m})$, $A_{\text{cs\_each}}$ is the cross-sectional area of the coil, and $2\pi r_{\text{cs\_each}}$ is the coil's circumference, where $r_{\text{cs\_each}}$ being the major radius of the coil. For all inner layer coils, $r_{\text{inner\_cs\_each}} = 88$ mm, and for all outer layer coils, $r_{\text{outer\_cs\_each}} = 100$ mm as shown in Figure 2-2 (a). The term $\pi a_{\text{cs\_each}}^2 - \pi a_{\text{cooling}}^2$ represents the cross-sectional area of the coil, where $a_{\text{cs\_each}}$ is the radius of the coil. For all inner and outer layer coils, $a_{\text{cs\_each}} = 5$ mm, and $a_{\text{cooling}} = 3.8\ mm$ is the radius of the hollow section in the coil, as shown in Figure 2-2 (a).

After obtaining the resistance of each single coil in each layer, we can calculate the total resistance of the central solenoid (R_{cs}) by summing them up:

$$\sum R_{\text{inner\_cs\_each}} + \sum R_{\text{outer\_cs\_each}} = R_{\text{cs}}. \tag{11}$$

For the vacuum vessel walls, we calculate the resistance of each single coil in Figure 2-2 (b) separately:

$$R_{\text{vessel\_each}} = \eta_{\text{stainless\_steel}} \frac{L_{\text{vessel\_each}}}{A_{\text{vessel\_each}}} = \eta_{\text{stainless\_steel}} \frac{2\pi r_{\text{vessel\_each}}}{a_{\text{vessel\_each}}^2} \tag{12}$$

where $R_{\text{vessel\_each}}$ is the resistance of a single coil in the vacuum vessel walls, $\eta_{\text{stainless\_steel}}$ is the resistivity of stainless steel $(7 \times 10^{-7}\ \Omega \cdot \text{m})$, $A_{\text{vessel\_each}}$ is the cross-sectional area of the coil, and $2\pi r_{\text{vessel\_each}}$ is the coil's circumference, where $r_{\text{vessel\_each}}$ is the major radius of the coil. For all inner vacuum vessel walls coils, $r_{\text{vessel\_each}} = 107$ mm, while for all the outer vacuum vessel walls coils, r_{vessel_each}

is calculated using Eq. (8), which ranges from 113 mm to 833 mm, as shown in Figure 2-2 (b). The term $a^2_{\text{vessel\_each}}$ represents the cross-sectional area of the coil, where $a_{\text{vessel\_each}}$ is the side length of the square coil. For all inner vacuum vessel walls coils, $a_{\text{vessel\_each}} = 2$ mm, while for all the outer vacuum vessel walls coils, $a_{\text{vessel\_each}} = 10$ mm, as shown in Figure 2-2 (b).

Figure 2-4 illustrates the resistance of each component. The first isolated point represents the central solenoid, while coil number 2 to 938 correspond to the inner vacuum vessel wall ring coils shown in Figure 2-2(b), starting from the bottommost ring coil and sequentially moving upward to the 937th ring coil. Since the inner vacuum vessel wall ring coils are identical in geometry, except for their z-coordinate, their resistance remains the same. Coil number 939 to 1125 correspond to the outer vacuum vessel wall ring coils in Figure 2-2(b), arranged from the bottommost coil up to the 188th ring coil. Unlike the inner vacuum vessel walls, the outer vacuum vessel wall ring coils have varying coil radius, causing their resistance to increase as the coil radius increases. As shown in Figure 2-4, the 94th coil in the outer vacuum vessel wall, which has the largest coil radius, also has the highest resistance.

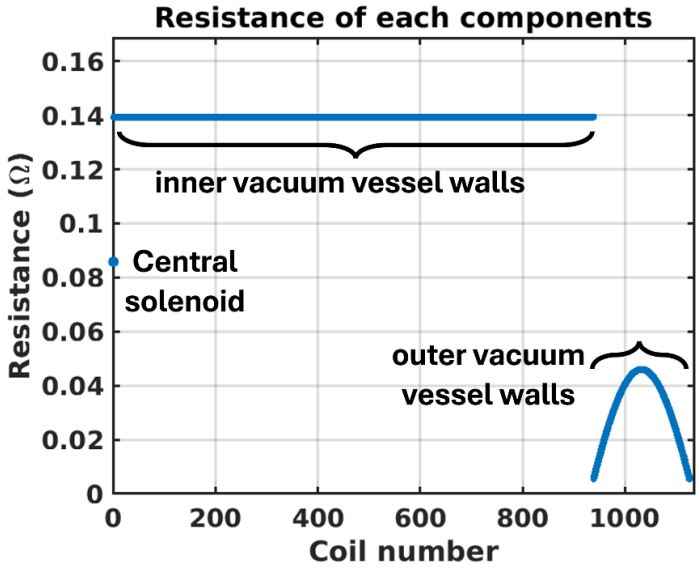

Figure 2-4: Resistance of each component

2.4.2. Calculation of self-inductance

In our calculations of inductance, all equations referenced below, along with their corresponding page numbers, equation numbers, or table numbers, are sourced from the book *Inductance Calculations: Working Formulas and Tables* by Frederick Grover [4]. One important point to note is that the calculations in the book are performed using units of centimeters, and the results obtained directly from the equations are in microhenries (μH). Therefore, it is crucial to ensure that the input units used in the equations and the output units from the results are consistent and properly accounted for.

For the central solenoid, we use the equation of solenoid self-inductance for the calculation [4]:

$$L_{\mathrm{cs}} = \mu_0 (\frac{N}{l})^2 Al = \mu_0 \frac{N^2}{l} A = \mu_0 \frac{N^2}{l} \pi r^2 \tag{13}$$

where L_{cs} is the self-inductance of central solenoid, μ_0 is the permeability of free space ($4\pi \times 10^{-7}\ {}^{H}/_{m}$), N is the total number of turns in the solenoid, l is the height of the solenoid, A is the cross-sectional area of the solenoid, and r is the major radius of the central solenoid, which is 94 mm, as mentioned in subsection 2.3.

For the vacuum vessel walls, the self-inductance of each single coil can be calculated using the known formula for the inductance of circular coils with square cross-sections, as given in Eq. 91 on page 95 of Ref. [4]:

$$L = 0.001 a N^2 P_0' \ \mu H \tag{14}$$

where L is the coil's self-inductance, and N is the number of turns in the coil. In our calculation, $N = 1$ since all components were cut into single coils. P_0' is a variable that can be calculated using Eq. 92 on page 95 of Ref. [4]:

$$P_0' = 4\pi \left\{ \frac{1}{2} \left[1 + \frac{1}{6} \left(\frac{a}{2r} \right)^2 \right] log_e \left[\frac{8}{\left(\frac{a}{2r} \right)^2} \right] - 0.84834 + 0.2041 \left(\frac{a}{2r} \right)^2 \right\} \tag{15}$$

where r is the major radius of the coil, and a is the side length of the coil.

Figure 2-5 illustrates the self-inductance of each component. The first isolated point represents the central solenoid, which has the highest inductance among all components due to its large number of turns and compact geometry. The self-inductance of coil number 2 to 938, corresponding to the inner vacuum vessel wall ring coils shown in Figure 2-2(b). These coils are arranged sequentially from the bottommost coil to the 937th coil. Since the inner vacuum vessel wall ring coils are geometrically identical except for their z-coordinate, their self-inductance values are the same. For coil number 939 to 1125, corresponding to the outer vacuum vessel wall ring coils, the self-inductance varies due to the increasing coil radius. As shown in Figure 2-5, the self-inductance peaks at coil 1032, which corresponds to the 94th ring coil of the outer vacuum vessel wall and has the largest radius.

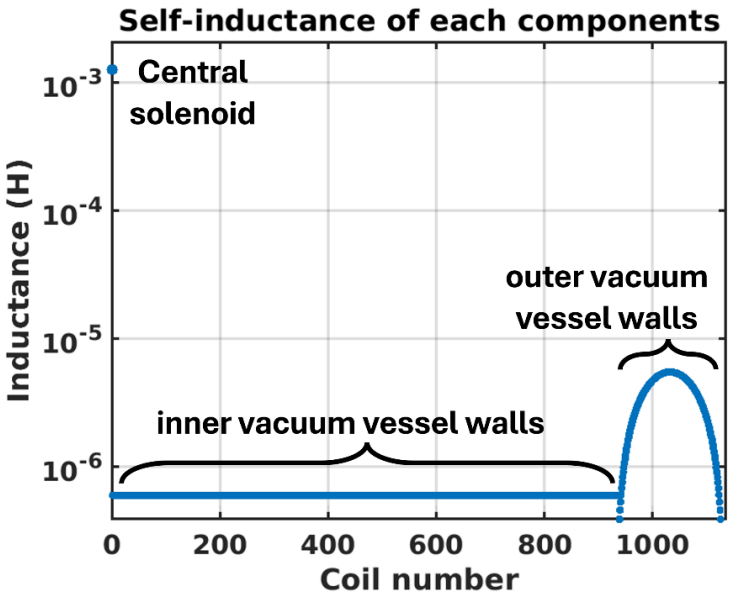

Figure 2-5 Self-inductance of each component

2.4.3. Calculation of mutual inductance

Our calculations consider all components, except for the central solenoid, as ring coils. Therefore, this sub-subsection has three sub-sub-subsections: (1) mutual inductance between vacuum-vessel-wall-ring coils and central solenoid; (2) mutual

inductance between the components of each vacuum vessel wall; and (3) calculation results of mutual inductance.

2.4.3.1. Mutual inductance between vacuum-vessel-wall-ring coils and central solenoid

Due to different vertical locations of the vacuum-vessel-wall ring coils, we categorize them into two groups. The first group consists of coaxial ring coils located between the top and bottom planes of the central solenoid, as shown in Figure 2-6. The second group consists of coaxial ring coils located either above the top plane or below the bottom plane of the central solenoid, as illustrated in Figure 2-7, which is the case for below the bottom plane of the central solenoid. For these two different cases, we employ different calculation methods for the mutual inductance between the central solenoid and the vacuum vessel walls.

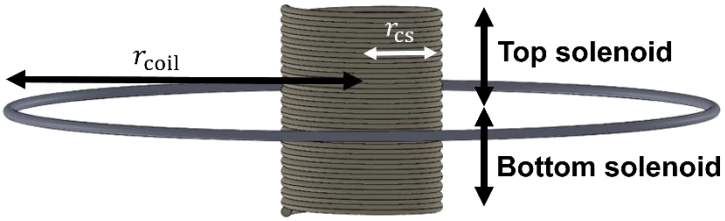

Figure 2-6: Coil schematic diagra

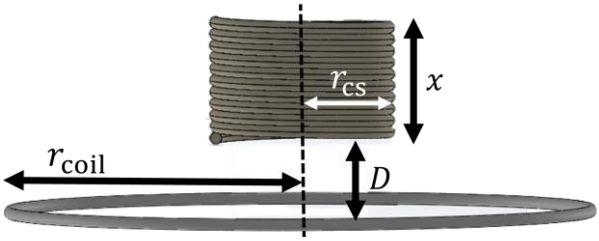

Figure 2-7: Coil schematic diagram

(1) Ring between the central solenoid

We first calculate the mutual inductance with the top and the bottom solenoid using Eq.(16). Then, the mutual inductance between the solenoid and the coaxial sing ring coil is the sum of them. When the single coil's plane is positioned between the top and bottom planes of the solenoid, as shown in Figure 2-6, the solenoid can be divided into two parts: the portion of the solenoid above the coil plane (referred to as the top solenoid) and the portion below the coil plane (referred to as the bottom solenoid). We can calculate the mutual inductance between the single coil and the top solenoid, as well as the mutual inductance between the single coil and the bottom solenoid. The sum of

these two mutual inductances gives the total mutual inductance between the main solenoid and the single coil.

The mutual inductance between a solenoid and a coaxial single coil located at its end plane can be calculated using the formula from Eq. 103 on page 115 of Ref [4]:

$$M = 0.002\pi^2 r_{\mathrm{cs}} \alpha \rho N Q_0 \tag{16}$$

where M is the mutual inductance between a solenoid and a coaxial single coil at its end plane, as illustrated in Figure 2-8. $N = 280$ in our calculation is the number of turns in the solenoid. Q_0 can be obtained from Table 27 in page 115 of Ref [4], r_{cs} is the major radius of the solenoid, which is 94 mm, as mentioned in subsection 2.3. The variable α can be calculated using the following equation:

$$\alpha = \frac{r_{\mathrm{cs}}}{r_{\mathrm{coil}}} \tag{17}$$

where r_{coil} is the major radius of the coil in Figure 2-8, corresponding to the r in Figure 2-2 (b) for each component of the vacuum vessel wall. The variable ρ can be calculated by:

$$\rho = \sqrt{\frac{{r_{\mathrm{coil}}}^2}{{r_{\mathrm{coil}}}^2 + x^2}} \tag{18}$$

where x is the distance between the top of central solenoid and the coil plane, as shown in Figure 2-8.

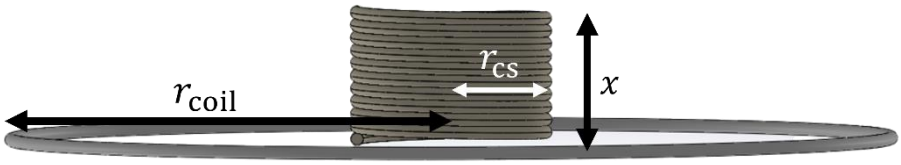

Figure 2-8: Coil schematic diagram

(2) Mutual inductance between a solenoid and a coaxial single coil with a distance D between the plane of the circle and the end of the solenoid

When calculating the mutual inductance between a coil and a solenoid, we treat the space between the solenoid and the coil as part of a solenoid, as illustrated by the light-

colored solenoid in Figure 2-8. We first calculate the mutual inductance $M_{\mathrm{x+D}}$ of the solenoid of length $(x + D)$, corresponding to the x and D Figure, and the single coil using Eq. (16). Then we calculate the mutual inductance of the solenoid of length D, corresponding to the D in Figure 2-7, and the single coil using Eq. (16) and get M_{D}.

Then, using three different conditions, we can calculate the mutual inductance between a solenoid and a ring coil at any position, provided that the two single coils are coaxial.

$$M_{\mathrm{x}} = M_{\mathrm{x+D}} - M_{\mathrm{D}}, \tag{19}$$

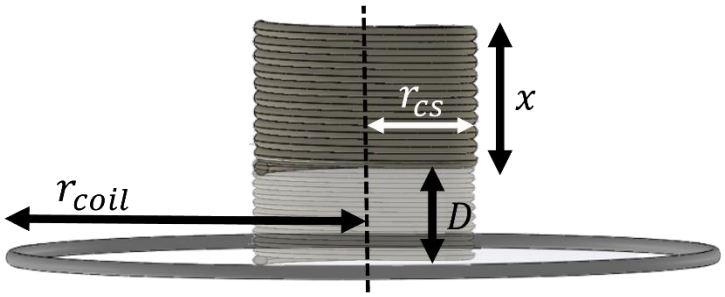

Figure 2-9: Coil schematic diagram

2.4.3.2. Mutual inductance between the components of each vacuum vessel wall

The mutual inductance between the components of each vacuum vessel, including the inner and outer vacuum vessel walls, can be calculated using the formula for the mutual inductance of coaxial circular filaments, as shown in Figure 2-10, as given in Eq. 77 on page 77 of Ref [4]:

$$M = f\sqrt{r_{\mathrm{c1}} r_{\mathrm{c2}}} \tag{20}$$

where M represents the mutual inductance of coaxial circular filaments. The value of f can be obtained from Table 13 on page 79 of Ref [4]. r_{c1} is the major radius of the smaller single coil, and r_{c2} is the major radius of the larger single coil, as shown in Figure 2-10.

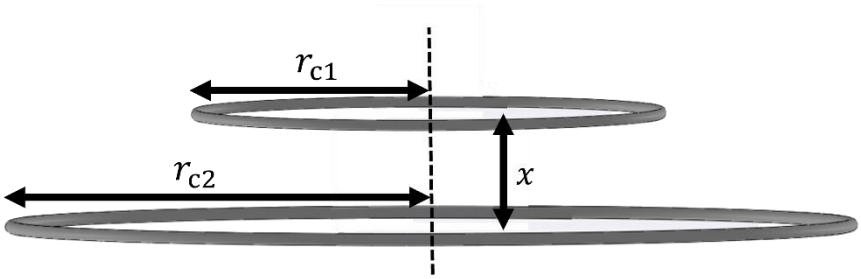

Figure 2-10: Coil schematic diagram

2.4.3.3. Calculation results of mutual inductance

Figure 2-11, as an example, illustrates the mutual inductance between all components and the 94th outer vacuum vessel wall ring coil (1032th coil in Figure 2-11), which corresponds to the middle outer vacuum vessel wall ring coil depicted in Figure 2-2(b). This coil has the largest radius among all outer vacuum vessel wall ring coils.

The mutual inductance values depend on the spatial relationship between the components and the 94th ring coil. The first data point represents the mutual inductance between the central solenoid and the 94th ring coil.

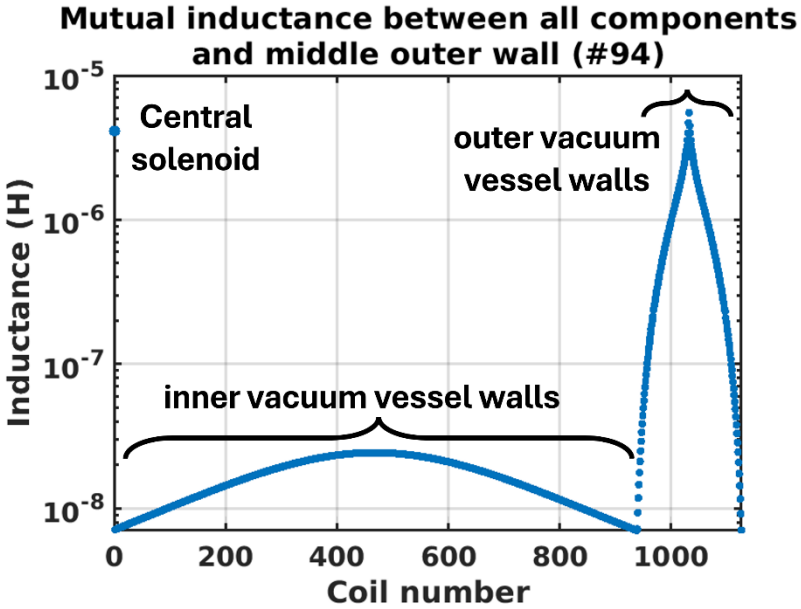

Figure 2-11: Mutual inductance between all components and the 94th outer vacuum vessel wall ring coil

For coil numbers 2 to 938, corresponding to the inner vacuum vessel wall ring coils, the mutual inductance gradually increases as the z-coordinates of these coils approach the plane of the 94th ring coil. This trend results from the geometric alignment

between these inner coils and the 94th ring coil.

For coil numbers 939 to 1125, representing the outer vacuum vessel wall ring coils, the mutual inductance peaks at the 94th ring coil itself, which is nearly equal to its self-inductance due to perfect alignment. Beyond this point, the mutual inductance decreases for coils located farther from the 94th coil due to increasing spatial separation, as illustrated in the plot.

Using Eq. (20), we can calculate not only the mutual inductance between each component of inner and outer vacuum vessel wall, but also the mutual inductance between vacuum vessel components and other coils, such as poloidal field coils, or the mutual inductance between two poloidal field coils, provided that the two single coils are coaxial.

Using Eq. (16) to (20), we can calculate the mutual inductance between the central solenoid and a coaxial single coil, as well as the mutual inductance between two coaxial single coils. Consequently, we can determine the mutual inductance between all components in our Tokamak and further calculate the induced currents between these components.

2.5. Calculated results

In our current calculations, we aim to determine the eddy currents in the inner and outer vacuum vessel walls induced by the time-varying current of the central solenoid. The calculation involves 937 ring elements in the inner vacuum vessel walls and 188 ring elements in the outer vacuum vessel walls, for a total of 1,125 vacuum vessel components. Including the central solenoid, there are 1,126 elements in total.

As a result, $\vec{V}_{\mathrm{cv}}$ will be represented as a column vector of size 1,126, as shown in Eq. (21). In Eq. (21), V_{cs} represents the time-varying voltage for central solenoid. The inner and outer vacuum vessel walls, however, do not have an external power source, so their voltage remains consistently zero:

$$\vec{V}_{\mathrm{cv}} = \begin{bmatrix} V_{\mathrm{c1}} \\ V_{\mathrm{v1}} \\ \vdots \\ V_{\mathrm{v1125}} \end{bmatrix} = \begin{bmatrix} V_{\mathrm{cs}} \\ 0 \\ 0 \\ \vdots \\ 0 \end{bmatrix}. \tag{21}$$

$\vec{I}_{\mathrm{cv}}$ will be represented as a column vector of size 1,126, as shown in Eq. (22). In Eq. (22), I_{c1} represents the time-varying current for central solenoid. I_{v1} to I_{v1125} represent the currents in the vacuum vessel components, which correspond to the eddy currents we aim to calculate:

$$\vec{I}_{\mathrm{cv}} = \begin{bmatrix} I_{\mathrm{cs}} \\ I_{\mathrm{v1}} \\ \vdots \\ I_{\mathrm{v1125}} \end{bmatrix}. \tag{22}$$

With $\overleftrightarrow{M}$ and $\overleftrightarrow{R}$ calculated in Subsection 2.3, we can determine the eddy currents in each ring element of the inner and outer vacuum vessel walls induced by the time-varying current in the central solenoid, using the provided central solenoid current profile shown as the red line in Figure 2-12 (a).

The calculated results of the eddy current distribution are presented in Figures 2-12(b) and 2-12(c). Since the inner and outer vacuum vessel walls are divided into several ring elements, Figure 2-12 (b) shows 937 eddy current lines corresponding to the 937 ring elements of the inner vacuum vessel walls. Similarly, Figure 2-12 (c) shows 188 eddy current lines corresponding to the 188 ring elements of the outer vacuum vessel walls.

By summing up the eddy currents from all 937 inner vacuum vessel wall ring elements, we can calculate the total eddy current generated in the entire inner vacuum vessel wall, represented as the blue solid line in Figure 2-11 (a). Similarly, by summing up the eddy currents from all 188 outer vacuum vessel wall ring elements, we can calculate the total eddy current generated in the entire outer vacuum vessel wall, represented as the blue dashed line in Figure 2-11 (a).

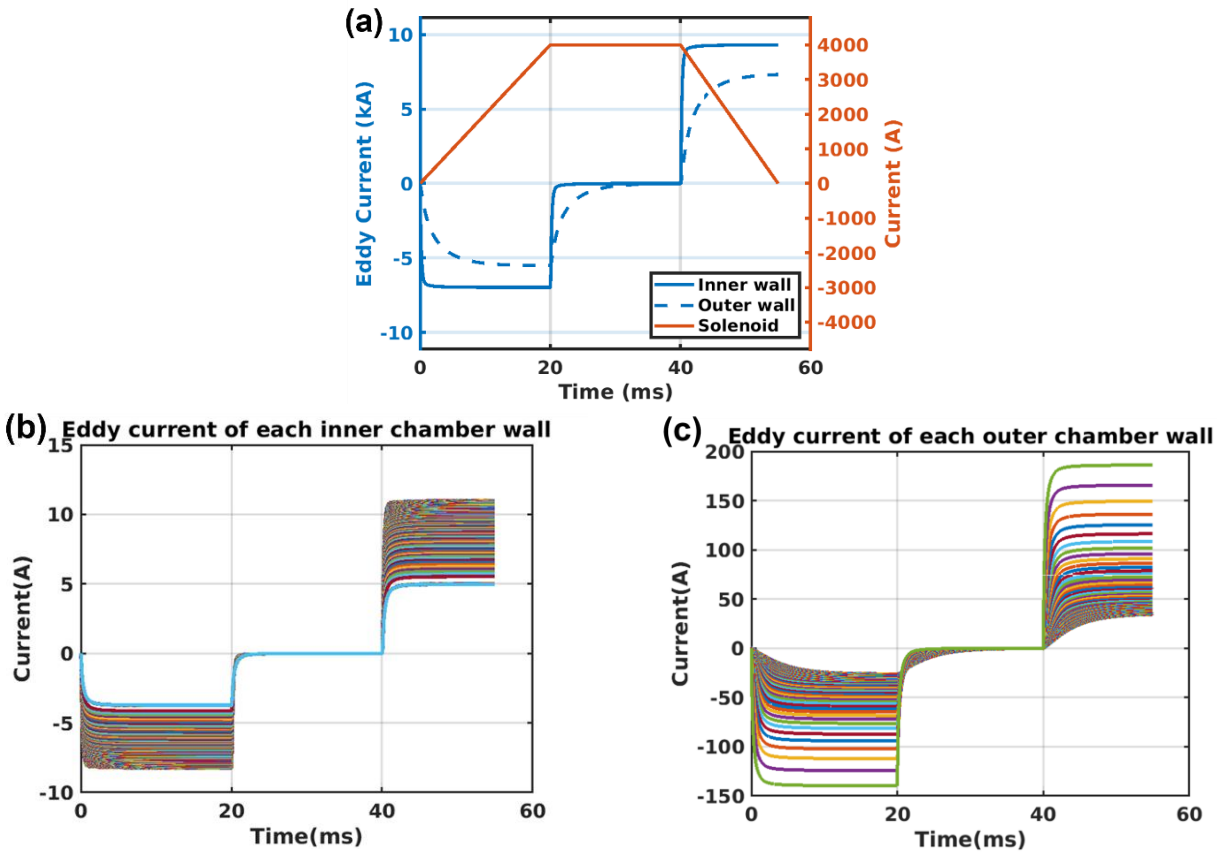

Figure 2-11: (a) Current profile of central solenoid and inner and outer vacuum vessel walls;
(b): Eddy current central solenoid induced in each inner vacuum vessel walls;
(c): Eddy current central solenoid induced in each outer vacuum vessel walls.

2.6. Conclusion

Through this algorithm, we can now calculate the eddy currents in the inner and outer vacuum vessel walls induced by the time-varying current of the central solenoid using Preconditioned Conjugate Gradient (PCG) method. By improving the condition number, PCG accelerates convergence, reducing the number of iterations needed while maintaining numerical stability. This is crucial as our matrix size increases with more calculated components, ensuring the computation remains scalable and efficient. This allows us to incorporate the influence of eddy currents into our subsequent design calculations to achieve more accurate results.

3. Loop voltage calculation

FIRST employs a central solenoid (CS) with driven by a time-varying current to produce a time-varying magnetic field. This field induces a loop voltage exceeding the breakdown voltage, which is necessary to ionize the gas and initiate plasma generation. The breakdown voltage is influenced by factors such as background pressure, connection length, and the plasma's position within the Tokamak.

The purpose of this section is to develop an algorithm to calculate the required loop voltage under varying conditions and determine the required central solenoid current rate to generate that loop voltage. It is to ensure that the central solenoid and the current profile that drives the central solenoid can meet the plasma generation demands, providing a critical basis for validating and optimizing the design. In addition, it helps identify potential design limitations and guides adjustments to improve the central solenoid's overall design.

This section consists of four subsections: (1) breakdown voltage for plasma generation; (2) the required central solenoid current rate; (3) calculation of the exact induced loop voltage; and (4) conclusion.

3.1. Breakdown voltage for plasma generation

As shown in Figure 3-1, plasma breakdown in a DC discharge occurs when the applied voltage across the anode (positive electrode) and the cathode (negative electrode) becomes sufficient to ionize the neutral gas molecules between the electrodes. The process begins with an initial ionization event near the cathode, where a free electron is liberated. This electron is accelerated by the electric field. If it has enough kinetic energy and collides with a neutral gas molecule, it may ionize it and release additional free electrons. All electrons including the original electron and these newly liberated electrons continue the process, leading to an exponential increase in the number of charged particles. The blue lines in the figure represent the paths of ionizing electrons,

while the orange lines represent the paths of liberated electrons. This cascading ionization process is known as the Townsend avalanche.

The connection length (L), marked by the vertical distance between the anode and cathode in Figure 3-1, defines the region within which the electric field acts to sustain the avalanche. This length directly impacts the number of ionization events that can occur before the electrons reach the anode. A longer connection length provides more chance for the avalanche to develop, increasing the total number of electrons and ions generated. Conversely, a shorter connection length limits the ionization path, reducing the amount of ionization.

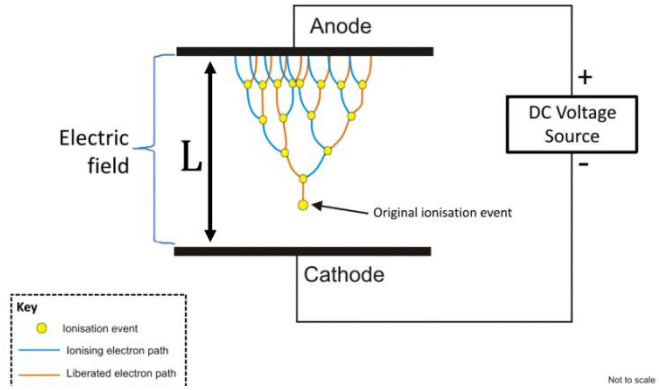

Figure 3-1: Visualization of Townsend Avalanche [5]

In contrast, there is no anode and cathode in the system to provide the electric field. A loop voltage in the azimuthal direction is generated by the central solenoid with time-varying current. Electrons gain energy from the loop voltage on the other hand, in the tokamak setup illustrated in Figure 3-2, the presence of an external toroidal magnetic field, applied by the toroidal magnetic field coils, determines the connection length. Unlike the finite connection length in Figure 3-1, the tokamak introduces a magnetic field (represented by the blue solid line in Figure 3-2) that forces electrons to gyro around the field line and move freely along them. Instead of being limited by a fixed physical distance between electrodes, the connection length in the tokamak becomes theoretically infinite because the electrons follow the closed-loop magnetic field lines

indefinitely. As a result, in the tokamak, free electrons are continuously gyring around the magnetic field line and collide with neutral gas molecules along the toroidal magnetic field line. This process ionizes the neutral gas and releases additional free electrons, sustaining a continuous avalanche.

In the Tokamak, we utilize the central solenoid to induce the discharge voltage, also known as the loop voltage or the applied voltage mentioned in Figure 3-1 in the previous paragraph, as shown in Figure 3-2. For an ideal solenoid, its magnetic field should be uniform and aligned along its central axis, as represented by the black solid line pointing downward in the middle of the solenoid in Figure 3-2. In reality, the solenoid produces stray magnetic field lines, as shown by the gray solid lines in Figure 3-2. These stray magnetic field lines cause the free electrons to deviate from the ideal toroidal path (the blue solid line in Figure 3-2). Instead of moving azimuthally along the toroidal magnetic field, electrons follow a helical path and move upward, as represented by the black solid line in Figure 3-3. Eventually, electrons collide with the outer vacuum vessel wall and are lost. This results in a finite connection length, in contrast to the infinite connection length observed in the ideal scenario.

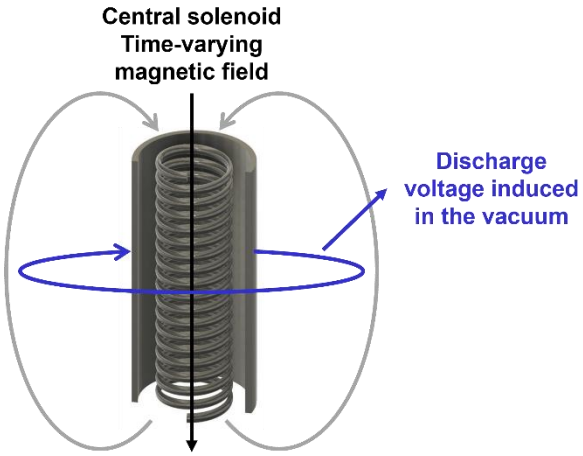

Figure 3-2: Stray magnetic field in a Tokamak

To calculate the connection length in our tokamak, we can straighten the black helical path of the electron in Figure 3-3, as represented by the hypotenuse of the

triangle in Figure 3-5. The opposite side of the triangle corresponds to the electron's displacement in the z-direction in Figure 3-3. Assuming the electron originates at a point 450 mm from the centerline at the bottom of the chamber and maintains the same distance from the centerline (450 mm) throughout its upward displacement, as shown by the black line in Figure 3-3, it eventually moves to the top of the chamber and is lost. In this case, since we already know the equation of the outer vacuum vessel wall curve, as shown in Eq. (23), which is an arc centered at x = -140 mm with an arc radius of 968 mm as illustrated in Figure 3-4. The opposite side equals the chamber height at the location 450 mm from the centerline can be calculated in Eq. (24), which is 1534 mm.

$$(x + 140)^2 + z^2 = 968^2 \tag{23}$$

$$y = \sqrt{968^2 - (450 + 140)^2} = 767 \text{ (at } x = 450\text{mm)}$$

$$\Rightarrow 2y = 1534\ mm \tag{24}$$

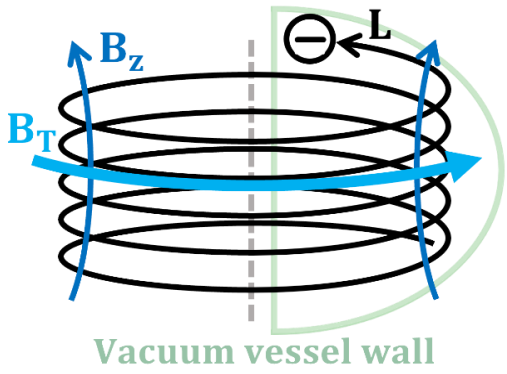

Figure 3-3: Realistic electron path in a

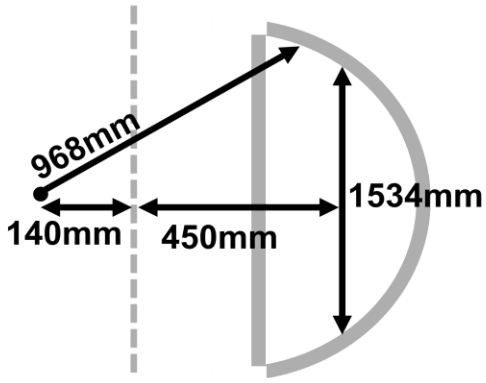

Figure 3-4: Connection length in Tokamak

The adjacent side of the triangle, side (a) in Figure 3-5 corresponds to the electron's displacement in the toroidal direction. The value $2\pi R$ represents the path length of one complete rotation along the toroidal magnetic field line at a distance R from the centerline. In our case, R is 450 mm. The total toroidal displacement depends on n, which represents the number of rotations the electron completes along the toroidal field line.

The adjacent side (side (a)) and opposite side (side (b)) of the triangle in Figure 3-5 correspond to B_T and B_Z in Figure 3-3, respectively, as they represent the effects of

B_T and B_Z on the electron's trajectory. Therefore, the ratio between the adjacent side and the opposite side equals to the ratio between B_T and B_Z. The smaller B_Z compared to B_T, the longer connection length L we can get.

Our goal is to ensure that B_Z is one-thousandth (1/1000) of B_T. Based on this ratio, if the opposite side length (corresponding to B_Z) in our calculation is 1534 mm, then the adjacent side length (corresponding to B_T) would be 1000 times greater, which is 1534 m.

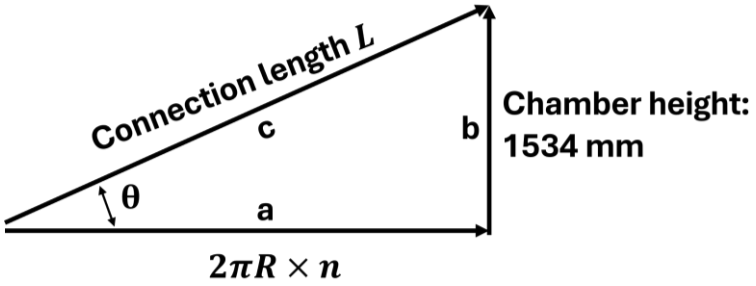

Figure 3-5: Realistic electron path in a tokamak magnetic

For the length of the hypotenuse (side (c)), if θ in Figure 3-4 is sufficiently small (less than 0.1°), the hypotenuse can be approximated as equal to the adjacent side. In our calculation, the opposite side of the triangle is one-thousandth (1/1000) of the adjacent side, so theta can be calculated as:

$$\theta = \arctan\left(\frac{\text{opposite}}{\text{adjacent}}\right) = \arctan\left(\frac{1}{1000}\right) = 0.057^{\circ}, \quad (25)$$

The result is approximately 0.057°, which satisfies the requirement. Therefore, the length of the hypotenuse can be considered the same as the length of the adjacent side, which is 1534 m, as calculated in the previous paragraph.

After calculating the connection length (L), we can determine the breakdown electric field (E_{BD}) using the Townsend coefficient (α), which describes the ionization rate of electrons as they travel through the gas. The physical meaning of α, the Townsend ionization coefficient, quantifies the number of ionization events caused by a single electron per unit length. For H_2 gas, the Townsend coefficient is given by [6]:

$$\alpha = A \cdot P_{H_2} \cdot \exp\left(\frac{-B \cdot P_{H_2}}{E}\right). \tag{26}$$

where $A = 3.83\ {}^{1}/_{m \cdot Pa}$ and $B = 93.6\ {}^{V}/_{m \cdot Pa}$ are the Townsend coefficient parameters for H_2, P_{H_2} is the gas pressure of H_2 in Pa, and E is the electric field strength. To achieve plasma breakdown, the product of the Townsend coefficient (α) and the connection length (L) must satisfy the following condition:

$$\alpha \cdot L > 1, \tag{27}$$

indicates that the number of ionization events occurring along the connection length (L) is sufficient to sustain a self-amplifying ionization process, leading to gas breakdown.

We combine Eq. (26) and Eq. (27) and apply some transformations to derive the minimum electric field required to achieve breakdown:

$$\begin{aligned} & A \cdot P_{H_2} \cdot \exp\left(\frac{-B \cdot P_{H_2}}{E}\right) \cdot L > 1 \\ \Rightarrow & \exp\left(\frac{-B \cdot P_{H_2}}{E}\right) > \frac{1}{A \cdot P_{H_2}} \\ \Rightarrow & \exp\left(\frac{B \cdot P_{H_2}}{E}\right) < A \cdot P_{H_2} \\ \Rightarrow & \frac{B \cdot P_{H_2}}{E} < \ln(APL) \\ \Rightarrow & E > \frac{B \cdot P_{H_2}}{\ln(APL)} \end{aligned} \tag{28}$$

The last term in Eq. (28) represents the condition for achieving breakdown, indicating that the induced electric field in the vacuum must be greater than $(B \cdot P_{H_2})/\ln(APL)$. Based on this condition, we can derive the breakdown electric field (E_{BD}) as:

$$E_{BD} = \frac{BP}{\ln(APL)} \tag{29}$$

where E_{BD} is the breakdown electric field, P is the gas pressure of H_2 in Pa, and L is the connection length.

Using the methods described above, we can calculate the breakdown electric field under different conditions, such as background pressure and connection length, which

depend on factors like the ratio between B_T and B_Z , the height of the chamber, and the distance from the centerline. Figure 3-6 shows the breakdown curve of the electric field for a gas pressure range from 10^{-4} Pa to 10^{0} Pa, with the ratio between B_T and B_Z varying from 0.1 to 0.001.

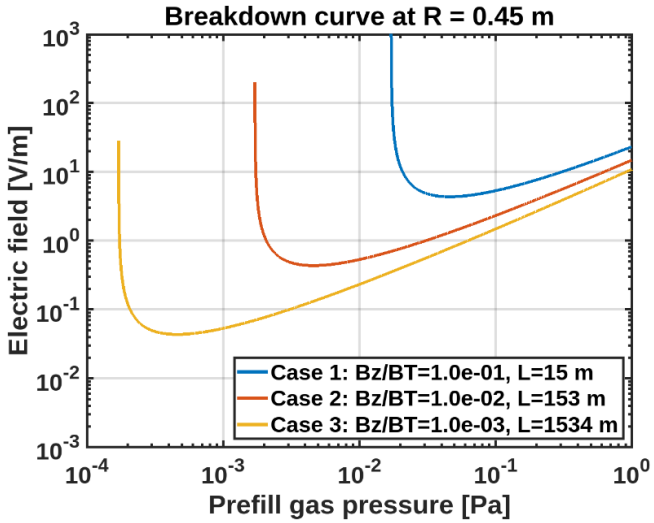

Figure 3-6: Breakdown electric field curve

By calculating the breakdown curve of the electric field, we can further determine the breakdown voltage (V_{BD}) at our desired plasma position:

$$V_{BD} = E_{BD} \cdot 2\pi R \tag{30}$$

where R is the distance from the centerline, which is 450 mm (0.45 m) in our present calculation. Figure 3-7 illustrates the breakdown voltage curve corresponding to the breakdown electric field shown in Figure 3-6.

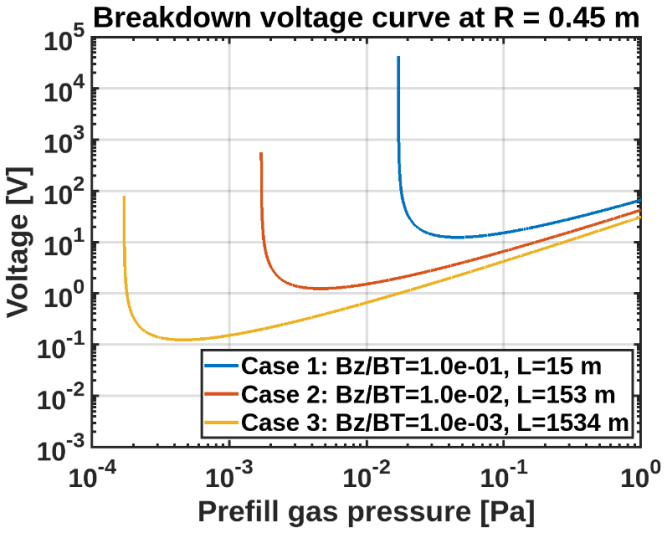

Figure 3-7: Breakdown voltage curve

3.2. The required central solenoid current charging rate

Using Eq. (29) and (30), we can calculate the breakdown voltage required to achieve breakdown under the target conditions of our experiment. For example, if the target condition is when B_z is 0.1% of B_t, and the chamber height is 1534 mm (at a radius of 45 cm), the connection length (L) is 1534 m. Additionally, if the pressure is 10^{-4} Torr (equivalent to 1.3×10^{-2} Pa), i.e., the particle density is approximately 10^{18} m^{-3}, the breakdown electric field is calculated using Eq. (29):

$$E = \frac{BP}{ln(APL)} = \frac{93.6 \times 1.3 \times 10^{-2}}{ln(3.83 \times 1.3 \times 10^{-2} \times 1534)} = 0.28\,{}^{V}/_{m}. \quad (31)$$

Based on this electric field, we can calculate the breakdown voltage required to generate plasma at a distance of 450 mm from the centerline using Eq. (30):

$$V = E \cdot 2\pi R = 0.28 \times 2\pi \times 0.45 = 0.8\ \text{V}. \quad (32)$$

Therefore, we can calculate the central solenoid current rate necessary to induce this voltage in the vacuum chamber.

The calculation of the central solenoid current rate required to induce the target loop voltage is based on Faraday's law of electromagnetic induction. According to Faraday's law, the induced voltage (V) in a loop is proportional to the rate of change of magnetic flux (φ) through the loop:

$$V = -\frac{d\varphi}{dt} \quad (33)$$

where V is the induced voltage (loop voltage), and φ is the magnetic flux. The magnetic flux (φ) is defined as:

$$\varphi = \int BdA \approx B \times A \quad (34)$$

where B is the magnetic field strength, and A is the cross-sectional area of the loop.

For an ideal solenoid, the magnetic field B can be expressed in terms of the current I:

$$B = \mu_0 \frac{N}{l} I \tag{35}$$

where μ_0 is the permeability of free space ($4\pi \times 10^{-7}\ {}^{H}/_{m}$), N is the number of turns in the coil, l is the length of the solenoid, and I is the current in the solenoid. Substituting B into the expression for φ (Eq. (34)):

$$\varphi = \mu_0 \frac{N}{l} I \times A. \tag{36}$$

By substituting the expression for φ into Faraday's law:

$$V = -\frac{d}{dt}\left(\mu_0 \frac{N}{l} I \times A\right). \tag{37}$$

Since μ_0, N, l, and A are constants, this simplifies to:

$$V = -\mu_0 \frac{N}{l} A \frac{dI}{dt}. \tag{38}$$

Rearranging to solve the rate of change of current $\left(\frac{dI}{dt}\right)$:

$$\frac{dI}{dt} = -\frac{V \cdot l}{r^2 \pi \cdot N \cdot \mu_0}. \tag{39}$$

To calculate the rate of change of current $\left(\frac{dI}{dt}\right)$ required to induce the target loop voltage, we substitute the given values into the derived formula:

- $V = 0.8\,V$: The target loop voltage that needs to be induced in the vacuum chamber, as calculated in Eq. (32).
- $l = 1.68\,m$: The axial length of the solenoid, where the magnetic field is distributed.
- $r = 0.094\,m$: The major radius of the solenoid, which is used to calculate the cross-sectional area, is mentioned in subsection 2.1.
- Cross-sectional area (A): The cross-sectional area of the solenoid is calculated as:

$$A = \pi r^2 = \pi(0.094)^2 = 0.314\,m^2. \tag{40}$$

- $N = 280$: The number of turns in the solenoid, contributing to the magnetic field strength.

- $\mu_0 = 4\pi \times 10^{-7}\ {}^{H}/_{m}$: The permeability of free space, a physical constant.

We get:

$$\frac{dI}{dt} = -\frac{0.8 \times 1.68}{\pi(0.1)^2 \cdot 280 \cdot 4\pi \times 10^{-7}} = -138\ {}^{A}/_{ms}. \quad (41)$$

The negative sign indicates that the current is decreasing over time, consistent with the direction of the induced voltage as described by Faraday's and Lenz's laws.

We developed a program to calculate the breakdown voltage under specific conditions. The program calculates the central solenoid current rate required to induce the breakdown voltage. After determining the current rate, the program can generate the central solenoid current profile by specifying the desired duration of the current, such as 15 ms, as shown in Figure 3-8. This profile is represented by the blue solid line in Figure 3-8 (a). Additionally, the program incorporates calculations from Section 2 to determine the eddy currents induced in the inner and outer vacuum vessel walls by the time-varying current of the central solenoid, based on the current profile. As shown in Figure 3-8 (a) the eddy current in the inner vacuum vessel walls corresponds to the red solid line, while the eddy current in the outer vacuum vessel walls corresponds to the red dashed line. Notice that the program first calculates the eddy current in each inner and outer vacuum vessel wall individually as shown in Figure 3-8 (b) and (c), respectively. The currents displayed in the Figure 3-8 (a) represent the total current, obtained by summing all the contributions from the inner walls and outer walls, respectively.

Through calculations, we determined that to induce a loop voltage of 0.8 V in a vacuum and maintain it for 15 ms, the maximum current of the central solenoid would be 2.1 kA. However, the 0.8 V breakdown voltage calculated in Eq. (30) represents the ideal conditions required for breakdown. In practice, various factors can influence the breakdown process. For example, if the actual B_z is greater than one-thousandth of

B_t, connection length would decrease, thereby increasing the required breakdown voltage. In this situation, generating only a 0.8 V loop voltage would not be sufficient to achieve breakdown and generate plasma.

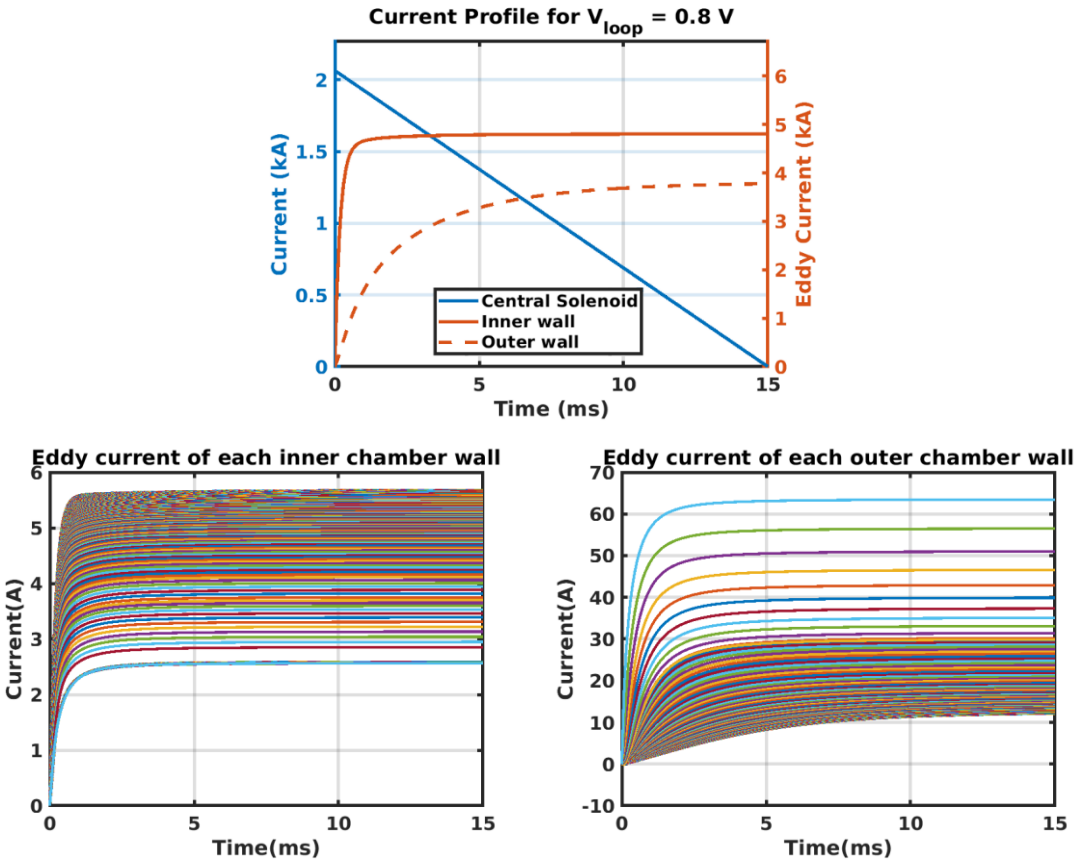

Figure 3-8: (a) Current profile of central solenoid and inner and outer vacuum vessel walls;
(b): Eddy current central solenoid induced in each inner vacuum vessel walls;
(c): Eddy current central solenoid induced in each outer vacuum vessel walls.

As a result, the induced loop voltage is often several times higher than the calculated breakdown voltage. Using this program, we can quickly calculate the maximum central solenoid current required for different loop voltages and durations. As shown in Table 1, if we aim to induce a 10 V loop voltage, the maximum current of the central solenoid would need to be approximately 20 kA. Alternatively, we can reduce the time duration ($t_{duratin}$) while maintaining the same current rate ($I_{max}/t_{duratin}$) to lower the required maximum current of the central solenoid.

This program allows us to verify whether the design of the central solenoid meets our requirements and helps us optimize the design accordingly.

Table 1: Central solenoid current requirements for different loop voltages and durations.

V_{loop}	$t_{duratin}$	I_{max}
$0.8\ V$	$15\ ms$	2.1 kA
$5\ V$	$15\ ms$	13 kA
$10\ V$	$10\ ms$	17 kA
$10\ V$	$15\ ms$	26 kA

3.3. Calculation of the exact induced loop voltage

Using the program described in Subsection 3.2, we calculated the current profile of the central solenoid and the individual coils of the inner and outer vacuum vessel walls. With the current profile, we can determine the magnetic field distribution produced by each coil representing the tokamak vacuum chamber element and further calculate the total magnetic flux. As shown in Eq. (33), the loop voltage is derived from the rate of change of magnetic flux. Notice that we only calculate the loop voltage in the equatorial plane. Therefore, by back-calculating from the magnetic flux variations, we can verify whether the current profile generated by the program in Subsection 3.2 can induce the required loop voltage in the vacuum.

First, we use the Biot-Savart Law to calculate the magnetic field distribution of each coil, which represents the vacuum vessel wall elements. It is important to note that since the tokamak is axisymmetric, the coils are also axisymmetric. Consequently, the magnetic field distribution only needs to be calculated in the xz-plane along the positive x-direction, as illustrated in Figure 3-9.

Similarly, for the central solenoid, we use the Biot-Savart Law to determine its magnetic field distribution. Due to its axisymmetric, the calculation can be restricted to the equatorial plane (i.e., z = 0 and y = 0). In this plane, the magnetic field component B_z lies along the positive x-direction, corresponding to the green line shown in Figure 3-9(b).

The equatorial plane (i.e., z = 0 and y = 0), represented by the gray circular plane in Figure 3-9(b), are chosen because the tokamak's axisymmetric structure ensures the magnetic field is symmetric about the central axis. By setting y = 0, we focus on the xz-plane containing this axis, while z = 0 corresponds to the midplane of the tokamak, equidistant from the top and bottom of the coils. This simplifies the calculations while fully capturing the magnetic field distribution.

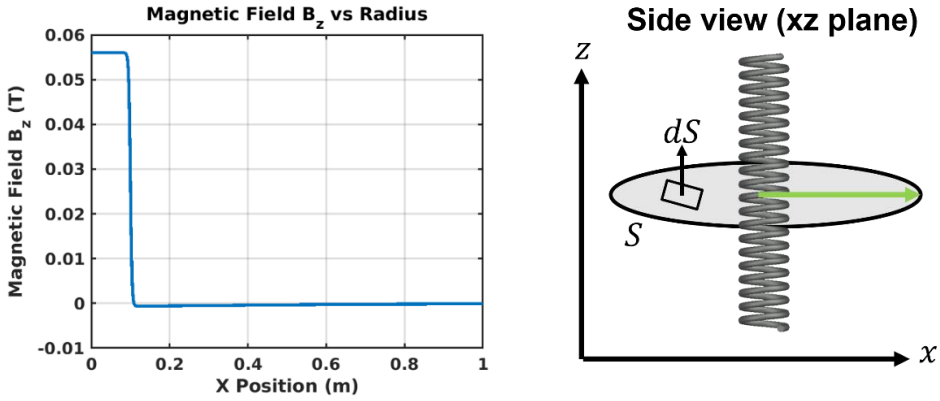

Figure 3-9: (a) Magnetic field B_z in the positive x-direction at z = 0 and y = 0; (b) Schematic of the central solenoid

Furthermore, only B_z is calculated because it is the only component of the magnetic field that is perpendicular the loop surface and determines the loop voltage in the tokamak.

After calculating the time-dependent changes in the magnetic field distribution, the magnetic flux (φ) can be determined by integrating the magnetic field along the green line, as shown in Figure 3-9(b). Since the tokamak is axisymmetric, the original surface integral can be simplified into a line integral. Instead of integrating over a surface area, we can integrate along a radial line and then multiply by the azimuthal symmetry factor $2\pi r$. This transformation allows us to express the flux calculation as:

$$\int B \cdot dA = \int B \cdot 2\pi r \cdot dr = 2\pi \int B \cdot r \cdot dr\,. \tag{42}$$

The integration results in the magnetic flux through the gray circular plane shown in Figure 3-9(b). The loop voltage is then calculated using Eq. (28):

$$V = -\frac{d\varphi}{dt}. \tag{43}$$

Using the above method, we calculated the loop voltage induced solely by the central solenoid current rate, as represented by the red line in Figure 3-8, which is 0.7 V. It is worth noting that the central solenoid current profile used for this calculation, as determined in Subsection 3.2, was designed to induce 0.8 V. The reason it only induces 0.7 V is that the calculations in Subsection 3.2 were based on ideal solenoid equations. However, in practical scenarios, various factors can reduce the induced loop voltage. Therefore, it is necessary to perform back-calculations to benchmark the accuracy and reliability of our calculations and to evaluate the performance of the central solenoid design.

Next, we applied the same approach to calculate the magnetic field distribution (B_z) produced by each single coil of the inner and outer vacuum vessel walls in the positive x-direction at z = 0 and y = 0. After summing these contributions, we integrated the total magnetic field to calculate the magnetic flux. Finally, using Eq. (33), we determined the loop voltage induced under the influence of eddy currents in the vacuum vessel walls, as represented by the blue line in Figure 3-10.

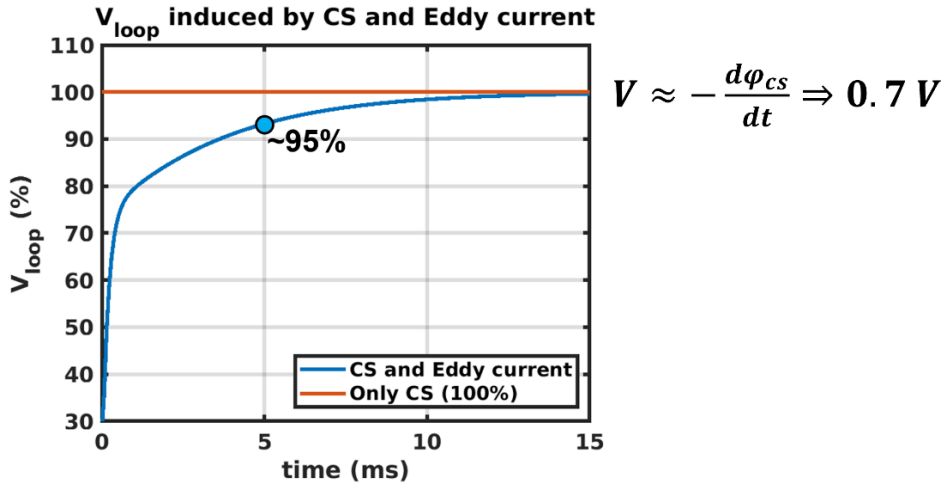

Figure 3-10: Comparison of loop voltage induced by central solenoid (CS) and eddy currents in the vacuum vessel walls over time

From Figure 3-10, it can be observed that around 5 ms, the influence of eddy currents in the vacuum vessel walls on the loop voltage reduces to approximately 5%. This is a key point as it indicates that designing a central solenoid current profile with a duration longer than 5 ms can significantly reduce the impact of eddy currents in the vacuum vessel walls on the loop voltage.

3.4. Conclusion

We have integrated the calculations from this subsection into a program, allowing us to quickly evaluate the loop voltage induced by the central solenoid current profile calculated in Subsection 3.2. The program also accounts for the effects of eddy currents in the vacuum vessel walls. This enables us to benchmark the accuracy and reliability of the calculations, as well as assess the performance of the central solenoid design. By doing so, we can further optimize the design to meet experimental requirements.

Through the calculations and programs, we can now determine the required breakdown voltage under different conditions. Additionally, we can quickly compute the central solenoid current profile needed to induce this loop voltage, as well as the resulting eddy currents in the vacuum vessel walls. Using the calculated current, we back-calculate the actual induced loop voltage to benchmark the accuracy and reliability of our calculations and evaluate the performance of the central solenoid design. This process enables us to further optimize the design to meet experimental requirements.

4. Calculation of the evolution of plasma parameters

In the previous section, we calculated the breakdown voltage required to generate plasma, the central solenoid current profile needed to induce the loop voltage in a vacuum, and the actual induced voltage. Based on these calculations, we assume that in the experiment, breakdown happened, plasma is generated, and the plasma can be modeled as a single-turn elliptical coil inside the vacuum chamber as shown in Figure 4-1. The elliptical cross-section of the coil is centered on the z = 0 plane, 450 mm from the centerline, which is the value used in Section 2 for our calculations. The minor axis of the coil is 32 cm. The elongation factor $\kappa = 2.4$, which represents the ratio of the major axis of the ellipse to its minor axis, gives the coil with the major axis of 76.8 cm.

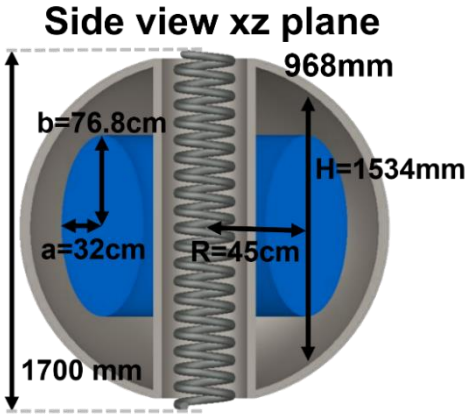

Figure 4-1: Simplified xz-plane cross-section of FIRST

As mentioned in Section 1, the full circuit equation, which accounts for mutual inductance, allows us to calculate the induced currents between various components within the tokamak device. Similarly, the plasma can be modeled as a single-turn coil, represented by the blue toroidal shape shown in Figure 4-1. By determining the plasma's resistance, self-inductance, and mutual inductance with other components, we can calculate the induced current within the plasma. In our current calculation, this induced current, primarily generated by the central solenoid, is also influenced by eddy currents in the vacuum vessel walls and can be referred to as the plasma current.

Once the plasma current is known, we can calculate the energy gained by the plasma through ohmic heating. Using this, we can determine the evolution of plasma parameters over time, such as plasma temperature and current. This analysis allows us to evaluate whether the designed central solenoid current profile can achieve our current experimental goals, which include a plasma temperature exceeding 100 eV and a plasma current greater than 100 kA. Based on these results, we can further design and adjust the central solenoid current profile to ensure the plasma parameters meet our targets.

This section consists of four sections: (1) calculation of plasma parameters; (2) calculation of the plasma current; (3) sensitivity test of the program to the initial temperature; and (4) Conclusion.

4.1. Calculation of plasma parameters

To calculate the plasma current, we first need to determine the plasma resistance and inductance. The self-inductance of the plasma can be calculated using the following equation [7]:

$$L_p = \mu_0 R \left(ln \frac{8R}{a} + \frac{l_i}{2} - 2 \right) \tag{44}$$

where L_p is the self-inductance of the plasma, μ_0 is the permeability of free space ($4\pi \times 10^{-7}\ {}^{H}/_{m}$), R is the distance from the centerline, which is 45 cm in our calculation and corresponds to R in Figure 4-1.The parameter a represents the minor radius of the plasma, which is 32 cm and corresponds to a in Figure 4-1. The parameter l_i, which represents the internal inductance of the plasma, is a function of the current distribution in the cross-section. In our calculation, $l_i = 0.5$.

As for the mutual inductance, since Eq. (16) and Eq. (20) depend only on the position of the coil filaments and is independent of the coil's minor radius, we can directly use it to determine the mutual inductance between the plasma and tokamak

components, as the plasma is coaxial with them. Finally, we obtained the necessary inductance for matrix $\overleftrightarrow{M}$ in the full circuit equation.

For matrix $\overleftrightarrow{R}$, since plasma parameters such as temperature and density change over time, they affect plasma resistance. Therefore, before calculating the plasma current, we must first determine how these plasma parameters evolve over time.

The plasma resistance can be calculated using the Spitzer equation [8]:

$$\eta_{Sp} = 5.2 \times 10^{-3} \cdot Z \cdot ln\Lambda \cdot T_e^{-1.5} \cdot 10^{-2}, \tag{45}$$

where η_{Sp} is the Spitzer resistivity, Z is the charge state of the ions; T_e is the electron temperature in electron volts (eV), and $ln\Lambda$ is the Coulomb logarithm [8], which can be determined by:

$$ln\Lambda = 23.5 - log\left(\frac{\sqrt{n_e \times 10^{-6}}}{T_e^{\frac{5}{4}}}\right) - \sqrt{10^{-5} + \frac{(log(T_e) - 2)^2}{16}}. \tag{46}$$

In our present experiment, we use H_2, so $Z = 1$.

The plasma resistance can be calculated using the Spitzer resistivity as follows:

$$R_p = \eta_{Sp}\frac{L}{A} = \eta_{Sp}\frac{2\pi R}{\pi ab} \tag{47}$$

where R_p is the plasma resistance, L is the effective length of the plasma current path, which is the length of the plasma coil of the blue toroidal shape single-coil shown in Figure 4-1 given by $2\pi R$, $R = 45$ cm is the major radius of plasma. The parameters $a = 32$ cm and $b = 76.8$ cm represent the minor and major axes of the plasma cross-section, respectively. The cross-sectional area of the plasma is given by $A = \pi ab$.

It can be observed that η_{Sp} and $ln\Lambda$ are affected by plasma density and temperature, both of them vary over time due to ionization and ohmic heating. Therefore, before calculating plasma resistance, we must first determine how ionization fraction and temperature evolve over time.

This section consists of two subsections: (1) calculation of plasma density; and (2) calculation of plasma temperature.

4.1.1. Calculation of plasma density

To calculate the plasma density, we first need to determine the ionization rate.

The initial ionization rate can be calculated using the ratio of electron-atom to electron-ion collision cross-sections [7]:

$$n_e \sigma_{e-i} = (n_a - n_e)\sigma_{e-a}, \tag{48}$$

where n_e is the electron density (m^{-3}), n_a is the total particle density (m^{-3}), which is related to the gas pressure of the experiment and is assumed constant, σ_{e-i} is the electron-ion collision cross-section , given by $\sigma_{e-i} \approx 1.5 \times 10^{-16} \times T_e^{-2}\ (m^2)$ [7], σ_{e-a} is the electron-atom collision cross-section, given by: $\sigma_{e-a} \approx 3 \times 10^{-19} \times T_e^{-0.5}\ (m^2)$ [7], T_e is the electron temperature (eV), and $(n_a - n_e)$ represents the neutral atom density, which can be approximated as n_0. The left-hand side of Eq. (48) represents the rate of electron-ion collisions, which is determined by the product of the electron density (n_e) and the electron-ion collision cross-section (σ_{e-i}). It means the neutralization rate and how fast ions are lost. The right-hand side represents the rate of electron-atom collisions, which depends on the neutral atom density ($n_a - n_e$) and the electron-atom collision cross-section (σ_{e-a}). It means the ionization rate and how fast ions are generated. Assuming equilibrium, neutralization rate equals to the ionization rate. Since the plasma density evolves due to ionization, this equation establishes the relationship between the electron population and the remaining neutral atoms based on their respective collision cross-sections.

By rearranging Eq. (48), we obtain:

$$\frac{n_e}{n_a - n_e} = \frac{\sigma_{e-a}}{\sigma_{e-i}} \approx \frac{3 \times 10^{-19}\, T_e^{-0.5}(eV)}{1.5 \times 10^{-16}\, T_e^{-2}(eV)} = 2 \times 10^{-3} \times T_e^{3/2}(eV) \text{ [7]}, \tag{49}$$

Since $n_e/(n_a - n_e)$ is proportional to $T_e^{3/2}$, it implies that higher electron

temperatures lead to a faster ionization process. This is because higher-energy electrons have a greater probability of ionizing neutral atoms upon collision. As a result, the plasma formation rate is heavily influenced by how effectively the system heats the electrons.

In our experiment, n_a should increase due to outgassing, a process where gas molecules trapped in the chamber walls or internal components are gradually released into the vacuum environment. As a result, outgassing introduces additional neutral atoms, affecting the overall particle density. However, for simplicity, in our current calculation, we assume n_a remains constant, neglecting the dynamic effects of outgassing. This allows us to focus on evaluating the fundamental relationship between electron density and temperature without additional complexities

At the early stage of plasma ionization, the number of electrons is still very low, meaning $n_a \gg n_e$. Initially, the neutral gas density n_a is much higher than the electron density n_e because the ionization process has just begun, and only a small fraction of atoms has been ionized, making the assumption of $n_a \gg n_e$ reasonable. Therefore, when calculating $n_a - n_e$, we can approximate it as n_a by neglecting n_e. This allows us to express the ionization rate as the ratio between n_e and n_a:

$$\gamma_c \approx \frac{n_e}{n_a} = 2 \times 10^{-3} \times T_{ec}^{\frac{3}{2}} \, (eV) \text{ [7]}, \tag{50}$$

However, it is important to note that this approximation is only valid during the early stage of plasma formation, where $n_a \gg n_e$. As the electron density increases and this condition no longer holds, we need to transition to a different calculation method to accurately describe the ionization process.

There are several methods for calculating the ionization rate. However, to save time and improve efficiency, we use precomputed rate coefficients derived from established models and theories in Atomic Data and Analysis Structure (ADAS).

Atomic Data and Analysis Structure [9] is a comprehensive database and toolset that provides accurate atomic and ionic data for modeling plasmas. It is widely used in fusion research, astrophysics, and laboratory plasma studies to ensure precise calculations of atomic processes, such as ionization, recombination, and radiation emission.

We can calculate the plasma density using the following equation:

$$\frac{dn_e}{dt} = R_{ion}(T_e, n_e)n_0 n_e - R_{rec}(T_e, n_e)n_e n_i. \quad (51)$$

The variable n_e represents the electron density, which is considered equivalent to the plasma density. The ion density, denoted as n_i, is assumed to be equal to the electron density ($n_i = n_e$) since ionization releases both an electron and an ion. The neutral atom density, n_0, is determined based on our calculations in Subsection 3.2, where the experimental pressure is 10^{-4} Torr (equivalent to 1.3×10^{-2} Pa). Given these conditions, the initial particle density is approximately $10^{18}\mathrm{m}^{-3}$, so we assume an initial neutral atom density of $n_0 = 10^{18}\ \mathrm{m}^{-3}$.

The effective ionization coefficient, denoted as $R_{ion}(T_e, n_e)$ [9], and the effective recombination coefficient, $R_{rec}(T_e, n_e)$ [9], both can be obtained from the ADAS database.

Eq. (51) represents the rate of change of electron density by accounting for both ionization and recombination processes. The first term describes electron generation due to ionization, while the second term accounts for electron loss due to recombination.

$R_{ion}(T_e, n_e)$ and $R_{rec}(T_e, n_e)$ are functions of the plasma temperature (T_e) and electron density (n_e), which we consider as the plasma temperature (T_p) and density (n_p)in our calculations. The electron temperature, displayed in eV, ranging from 0.2 eV to 1×10^4 eV. The electron density, ranging from $5\times10^{13}\ \mathrm{m}^{-3}$ to $2\times10^{21}\ \mathrm{m}^{-3}$.

Our current experiment aims to achieve a plasma temperature of 100 eV, with an

expected particle density in the range of 10^{17} m^{-3} to 10^{20} m^{-3}. Since these values fall within the range of the ADAS data, we can directly use this dataset for our calculations.

It is important to note that the ADAS data only provides particle densities starting from 5×10^{13} m^{-3}. Therefore, when our program calculates the plasma density, we adopt a two-step approach to account for the early-stage breakdown process. During the initial phase of plasma breakdown, we use Eq. (50), referred to as the collision model, to calculate the ionization rate. Once the electron density reaches 10% of the total particle density, we gradually transition to using Eq. (51), known as the ADAS model, by applying a weighted interpolation method.

Specifically, we define a transition parameter γ, where $\gamma = 0$ represents the early breakdown stage, and $\gamma = 0.4$ marks the point where the ADAS model fully takes over as shown in Figure 4-3. The weighting function ensures a smooth transition between the two models: when $\gamma = 0$, the collision model is fully applied with a weight of 100% ($w_{\gamma\_collision} = 1$) and the ADAS model has no contribution ($w_{\gamma_{scd/acd}} = 0$). As γ increases, the weight of the collision model gradually decreases, while the ADAS model weight increases accordingly. At $\gamma = 0.4$, the transition is complete, with $w_{\gamma\_collision} = 0$ and $w_{\gamma_{scd/acd}} = 1$. This interpolation method ensures a smooth and numerically stable switch between models, improving the accuracy of plasma ionization dynamics calculations.

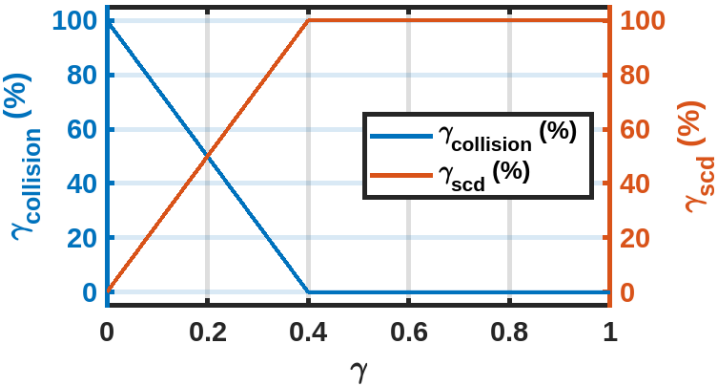

Figure 4-3: Central solenoid and plasma current profile

By implementing this approach, we can accurately calculate the time-dependent evolution of plasma density, maintaining physical consistency across different phases of ionization.

4.1.2. Calculation of plasma temperature

The change in electron energy (thermal energy) is determined by the balance between heating and power losses. Therefore, to calculate the time-dependent variation of plasma temperature, we use the following equation:

$$\frac{3}{2}\frac{d(n_e T_e)}{dt} = P_{oh} - (P_{ion} + P_{line}), \tag{52}$$

where $\frac{3}{2}n_e T_e$ represents the total energy per volume, P_{oh} represents the energy per volume generated by Ohmic heating, P_{ion} accounts for energy lost per volume due to ionization, as some of the input energy is used to ionize neutral atoms rather than increasing the electron temperature, and P_{line} represents energy loss per volume due to radiation, particularly line radiation from excited ions that emit photons as they transition between energy states.

The parameter P_{oh} in Eq. (52) represents the energy per volume generated by Ohmic heating, which we consider as the primary power input to the plasma. It is calculated as:

$$P_{oh} = \frac{I_p^2 R_p}{V_p} \left(\mathrm{W}/\mathrm{m}^3\right), \tag{53}$$

where I_p is plasma current (A), R_p is plasma resistance (Ω) given in Eq. (47), and V_p is plasma volume (m^3).

The parameter P_{ion} in Eq. (52) represents ionization loss, which is the energy required to remove an electron from a neutral atom. It is given by:

$$P_{ion} = R_{ion} \times n_e \times n_0 \times E_i \left(\mathrm{W}/\mathrm{m}^3\right), \tag{54}$$

where R_{ion} is the effective ionization coefficient, obtained from ADAS data [9], n_e

is the electron density, n_0 is the neutral atom density, and E_i is the ionization energy, which is the energy required to remove an electron from a neutral atom. For hydrogen $E_\mathrm{i} = 13.6$ eV. This equation is valid because each ionization event requires a fixed amount of energy (E_i) per ionized atom. The rate of ionization events is proportional to R_ion, which depends on plasma temperature and density. Since ionization involves collisions between electrons and neutral atoms, the energy loss rate is determined by the product of electron density, neutral atom density, and ionization energy per ion.

The parameter P_line in Eq. (52) represents line radiation loss, which occurs when excited atoms or ions transition between bound energy levels, emitting photons that escape the plasma. It is given by:

$$P_\mathrm{line} = R_\mathrm{plt} \times n_\mathrm{e} \times n_\mathrm{i} \ \left(\mathrm{W}/\mathrm{m}^3\right), \tag{55}$$

where R_plt is the coefficient of line emission from excitation, obtained from ADAS data [9], n_e is the electron density, n_i is the ion density and as mentioned before, we assume as $n_\mathrm{i} = n_\mathrm{e}$. This equation is based on the fact that line radiation occurs when electrons excite ions to higher energy levels, and these ions then emit photons upon returning to lower energy states. The excitation rate depends on electron-ion interactions, making the emission power proportional to the electron and ion densities.

This approach allows us to describe the energy balance in a plasma by considering both power input (Ohmic heating) and power losses (ionization and radiation losses). By utilizing this approach, we can compute how electron temperature evolves over time.

4.2. Calculation of the plasma current

After deriving the equations for plasma density and plasma temperature in Subsection 4.1, we only need to provide the initial conditions, including the initial plasma temperature, experimental gas pressure, and central solenoid current profile, to

compute the plasma parameters at each time step using the previously established equations.

In our calculation, we set the initial plasma temperature to 0.026 eV (~300 K), which corresponds to the room temperature. We apply the central solenoid current profile as shown by the black line in Figure 4-4.

We then compute the time evolution of plasma parameters under two different gas densities:

(1) 10^{18} m^{-3} (corresponding to P ~ 10^{-4} Torr), represented by blue-colored curves

(2) 10^{17} m^{-3} (corresponding to P ~ 10^{-5} Torr), represented by red-colored curves

The results for each case are presented in Figures 4-4 to 4-9, illustrating how plasma parameters evolve over time under these conditions。

From Figure 4-4, we observe that with an initial temperature of 0.026 eV (~300 K) and a central solenoid current profile starting from 10 kA and linearly decreasing to 0 kA within 10 ms, the plasma current exceeds the target value of 100 kA for both P = 10^{-4} Torr and P = 10^{-5} Torr. This suggests that Ohmic heating from the present current central solenoid profile is sufficient to drive the required plasma current.

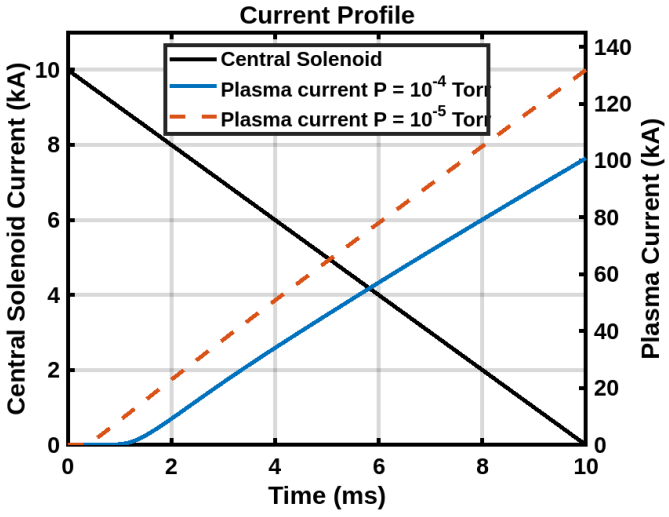

Figure 4-4: Central solenoid and plasma current

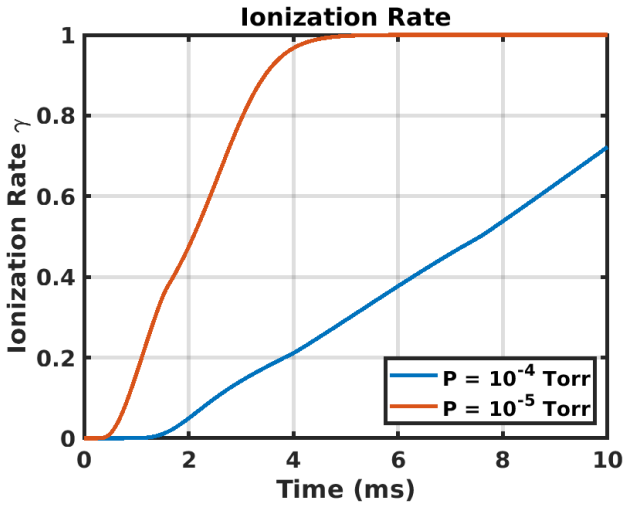

Figure 4-5: Ionization rate

Figure 4-5 shows that under P = 10^{-5} Torr, the plasma reaches full ionization at approximately 5 ms. However, for P = 10^{-4} Torr, the ionization process takes longer, as

the higher gas density results in more neutral particles that need to be ionized.

Regarding the plasma temperature in Figure 4-6, the case with P = 10^{-5} Torr successfully reaches the target temperature of 100 eV within the given central solenoid current profile. In contrast, for P = 10^{-4} Torr, the temperature only reaches 40 eV because more particles need to be heated, requiring additional energy input.

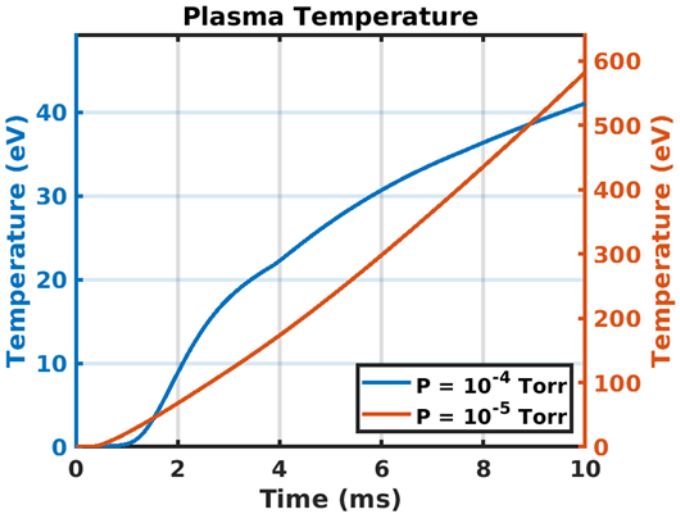

Figure 4-6: Plasma temperature

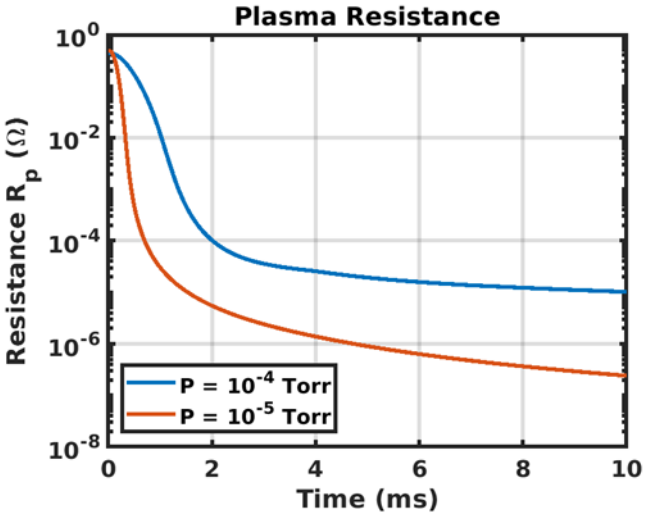

Figure 4-7: Plasma resistance

According to Eq. (38) and Eq. (40), plasma resistance R_p, which is shown in in Figure 4-7, is proportional to the Spitzer resistivity η_{Sp} and inversely proportional to the plasma temperature $T_{\mathrm{e}}^{1.5}$:

$$R_{\mathrm{p}} \propto \eta_{\mathrm{Sp}} \propto \frac{1}{T_e^{1.5}}. \tag{56}$$

Since the plasma temperature is higher for P = 10^{-5} Torr, its plasma resistance is lower than that of P = 10^{-4} Torr. The higher resistance in the P = 10^{-4} Torr case means that a greater loop voltage is required to sustain the same plasma current. This suggests that in experiments with higher gas pressures, more power is needed to maintain current flow, making plasma heating and sustainment more challenging.

Figure 4-8 shows the plasma energy loss, including P_{ion} (ionization loss) and P_{line} (radiation loss). For P = 10^{-4} Torr, both P_{ion} and P_{line} are larger than in the P = 10^{-5} Torr case due to two key factors.

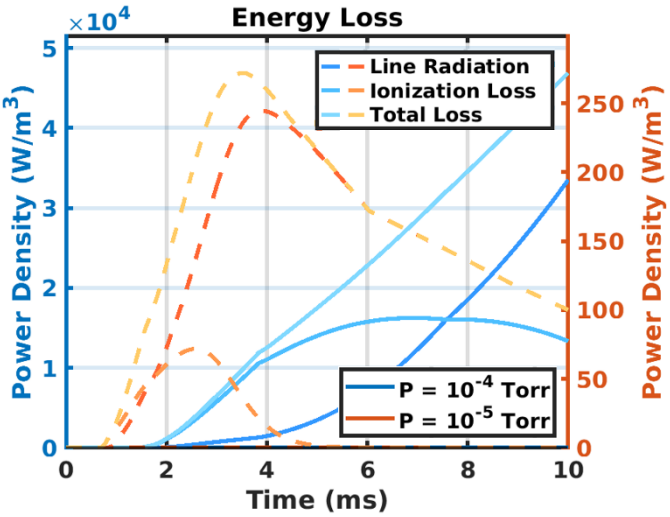

Figure 4-8: Energy loss

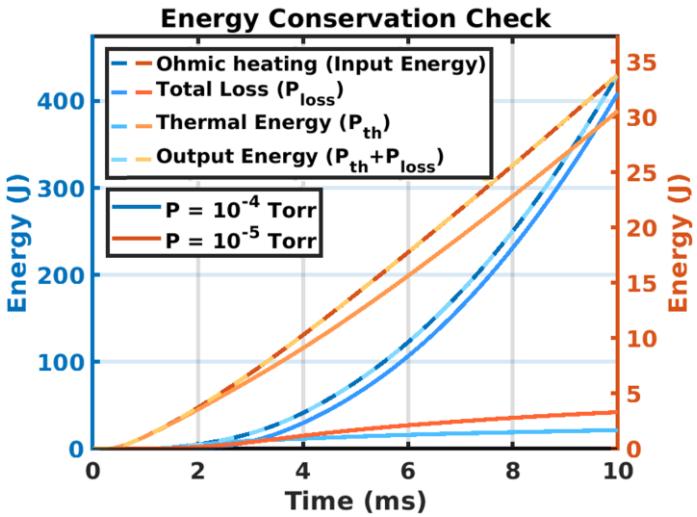

Figure 4-9: Energy conservation check

First, the higher gas density in P = 10^{-4} Torr leads to greater ionization loss. Since $P_{\text{ion}} \propto n_0 n_e$, a higher initial neutral density (n_0) results in more frequent ionization events, causing a greater overall loss of energy required for ionization.

Second, the higher particle density in P = 10^{-4} Torr contributes to greater radiation loss. Since line radiation (P_{line}) is proportional to $n_e n_i$, a denser plasma leads to more frequent electron-ion collisions, which in turn increase excitation events and subsequent photon emissions.

Figure 4-9 demonstrates that the calculations performed by the program satisfy energy conservation. The Ohmic heating from the central solenoid serves as the energy input to the plasma, which is the darkest-colored line in Figure 4-9.

To calculate the total energy input, we first convert Eq. (53) into total input power (W) by multiplying by the plasma volume (V_p):

$$P_{\text{oh}} = \frac{I_p^2 R_p}{V_p} \left(\text{W}/\text{m}^3\right) \Rightarrow P_{\text{oh}} V_p \text{ (W)} \tag{57}$$

where I_p is plasma current (A), R_p is plasma resistance (Ω), and V_p is plasma volume (m^3). Next, to determine the total accumulated energy input over time, we integrate P_{oh} from $t = 0$ to the current time $t = 15$ ms:

$$E_{input} = V_{\mathrm{p}} \int_0^t P_{oh} dt \approx V_{\mathrm{p}} \sum_{i=1}^{n} P_{oh}(i) \cdot \Delta t \tag{58}$$

where E_{input} is the total accumulated energy input to the plasma over time (J), $P_{oh}V_{\mathrm{p}}$ is the Ohmic heating power (W), and Δt is the time step used for numerical integration.

The total energy loss of the plasma in Figure 4-9 is the sum of P_{ion} (ionization loss) and P_{line} (radiation loss). The ionization loss corresponds to Eq. (54) and accounts for the energy required to ionize neutral atoms. The radiation loss corresponds to Eq. (55) and represents the energy lost due to photon emission from electron-ion interactions.

The net energy retained by the plasma is given by the equation:

$$U = \frac{3}{2} n_{\mathrm{e}} \cdot V_{\mathrm{p}} \cdot T_{\mathrm{e}} \times eV\_to\_J \tag{59}$$

where U represents the internal energy of the plasma, measured in joules (J), which quantifies the total thermal energy stored within the plasma. The term n_{e} refers to the electron density. The variable V_{p} represents the plasma volume (m^3). The term T_{e} represents the plasma temperature, measured in electron volts (eV), which describes the thermal energy per particle in the plasma. The final term, eV_to_J, is a conversion factor from electron volts to joules, with a value of $1.6 \times 10^{-19}\ J/eV$.

As shown in Figure 4-9, the input energy from Ohmic heating is equal to the total output energy, which includes thermal energy and energy losses. This balance ensures that the program correctly accounts for energy input, dissipation, and conversion, thereby confirming that energy conservation is maintained within the simulation.

4.3. Sensitivity test of the program to the initial temperature

Before utilizing the program in Subsection 4.2 to further refine the design of the central solenoid current profile, we first need to test the program's sensitivity to the

initial temperature. This verification is important because the initial temperature serves as a critical starting condition for plasma evolution. Since the governing equations for plasma density, temperature, and resistance all involve temperature-dependent terms, variations in the initial temperature could impact the overall plasma dynamics. By testing the program's response to different initial temperatures, we can ensure that the numerical simulation remains stable and consistent, regardless of the initial condition chosen.

This sensitivity test allows us to evaluate whether small variations in the initial temperature lead to significantly different plasma behavior, which could indicate potential uncertainty in the model. If the simulation remains consistent under different initial temperature conditions, we can confidently proceed to use the program for further optimization of the central solenoid current profile. We performed calculations under different initial temperature conditions, setting T_0 = 0.2 eV, 5 eV, and 50 eV, as shown in Figure 4-10 and Figure 4-11.

As observed in Figure 4-10, when the initial plasma temperature is relatively high (e.g., 20 eV), it first decreases before rising. This occurs because at higher temperatures, energy losses due to line radiation, ionization, or radiation dissipation can exceed Ohmic heating. Consequently, the net power, defined as $P_{net} = P_{oh} - P_{loss}$, may initially become negative, leading to a drop in temperature. Over time, as electron density and plasma resistance evolve, Ohmic heating increases, eventually surpassing the losses and driving the temperature back up, resulting in the observed downward-then-upward trend.

Additionally, this initial temperature drop reduces the ionization rate, as shown in Figure 4-11, since ionization is strongly temperature-dependent. Ultimately, as the current and resistance evolve, Ohmic heating "catches up" with energy losses, stabilizing and increasing the temperature again.

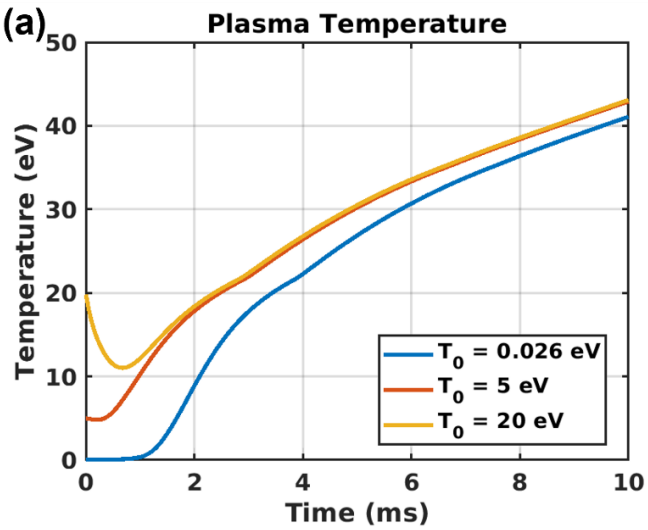

Figure 4-10: Plasma temperature

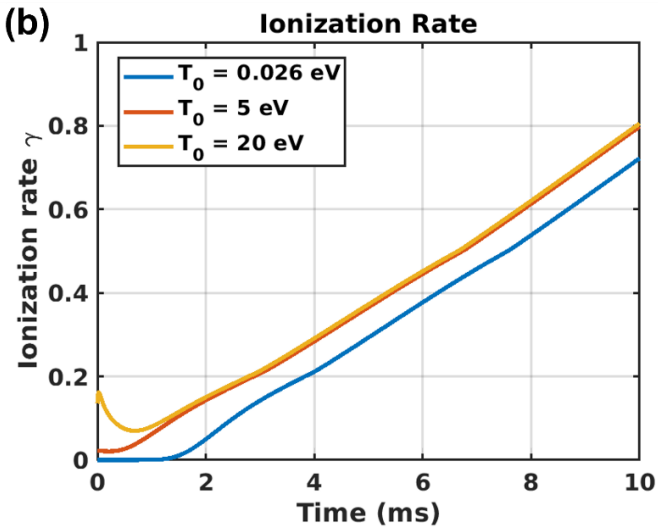

Figure 4-11: Ionization rate

We can observe that in Figure 4-10 and Figure 4-11 the plasma temperature and ionization rate result for the three different initial temperatures ultimately converge. This convergence occurs because the net heating power and energy loss in the plasma reaches a dynamic balance over time, driving the system toward a similar final temperature and ionization rate regardless of the initial condition.

This behavior can be attributed to several mechanisms. Plasma resistance decreases as the temperature rises, particularly with higher electron temperatures. At higher temperatures, the lower resistance reduces the effectiveness of Ohmic heating ($P_{\mathrm{oh}} = I_{\mathrm{p}}^2 R_{\mathrm{p}}/V_{\mathrm{p}}$), while at lower initial temperatures, higher resistance leads to stronger Ohmic heating, accelerating the temperature increase in the early stages.

Additionally, energy loss mechanisms such as line radiation and ionization losses become more significant at higher temperatures. For higher initial temperatures, these losses can temporarily exceed Ohmic heating, resulting in a negative net power ($P_{\mathrm{net}} = P_{\mathrm{oh}} - P_{\mathrm{loss}}$) and causing a temperature drop, as shown in the yellow line for 20 eV case in Figure 4-10. In contrast, for lower initial temperatures, Ohmic heating dominates over losses, leading to a faster temperature rise.

As the plasma evolves, a balance is eventually established between Ohmic heating

and energy losses. This equilibrium determines the final temperature range and is primarily influenced by the system's injected power, geometry, density, and radiative properties, rather than the initial temperature. Therefore, whether the plasma starts at 0.026 eV, 5 eV, or 20 eV, the temperature trajectories converge, with differences only in the early transitional behavior. Over longer timescales, the equilibrium between Ohmic heating and energy loss mechanisms governs the plasma's steady-state temperature.

In conclusion, through this calculation, we have demonstrated that our program has low sensitivity to the initial plasma temperature. This reliability allows us to proceed further refining the design of the central solenoid current profile using the program.

4.4. Conclusion

In this section, we developed and validated a program capable of calculating the evolution of various plasma parameters, including temperature, current, and resistance. We also tested the program's sensitivity to the initial plasma temperature and confirmed its robustness. By using this program, we can optimize the central solenoid current profile and refine hardware designs to ensure that the plasma temperature and current meet our experimental objectives.

5. Future work

In the first half of 2025, I will design a central solenoid current profile that aligns with the hardware specifications of the FIRST tokamak device and ensures that the plasma temperature in the P = 10^{-4} Torr case reaches 100 eV. At the same time, our laboratory is constructing its own mini tokamak, for which I will use the programs developed in this report to assist in its design. Additionally, I will utilize simulation tools such as FreeGS to calculate the equilibrium state of the mini tokamak.

6. Conclusion

In 2024, I developed a series of computational programs to calculate and optimize key parameters of the FIRST tokamak device. These programs focused on calculating eddy currents in the vacuum vessel walls, determining the required loop voltage for plasma generation, and modeling the time-dependent evolution of plasma parameters.

Through these calculations, we established a valid framework for predicting plasma behavior and optimizing the central solenoid current profile. Sensitivity tests confirmed that our program remains stable across different initial conditions, ensuring its reliability for further applications.

In 2025, I will use these programs to refine the central solenoid current profile to achieve a 100 eV plasma temperature in the P = 10^{-4} Torr case. Additionally, as our laboratory is constructing a mini tokamak, I will apply these models to assist in its design and simulate its equilibrium state using FreeGS.

Reference

[1] Po-Yu Chang. 國科會磁約束高溫電漿計畫-子計畫一執行情形

[2] H.-T. Kim *et al.*, *Nuclear Fusion*, 62, 126012 (2022) "Development of full electromagnetic plasma burn-through model and validation in MAST"

[3] https://www.mathworks.com/help/matlab/ref/pcg.html

[4] F. W. Grover, *Inductance Calculations: Working Formulas and Tables*. New York: D. Van Nostrand Company, 1946

[5] Dougsim, "Secondary electrons," Wikipedia, [Online]. Available: https://en.wikipedia.org/wiki/Secondary_electrons. [Accessed: Feb. 10, 2025].

[6] P. C. de Vries and Y. Gribov, *Nuclear Fusion*, 59, 096043 (2019), "ITER breakdown and plasma initiation revisited"

[7] H.-T. Kim *et al*., *Nuclear Fusion*, 52, 103016 (2012), "Enhancement of plasma burn-through simulation and validation in JET"

[8] F. Trintchouk *et al, Physics of Plasmas*, 10, 319 (2003), "Measurement of the transverse Spitzer resistivity during collisional magnetic reconnection"

[9] ADAS – Atomic Data and Analysis Structure, *ADAS*, [Online]. Available: https://open.adas.ac.uk/. [Accessed: Feb. 10, 2025].